Estimation of Particulate Backscattering Coefficient in Turbid Inland Water Using Sentinel 3A-OLCI Image

Jiafeng Xu, Yingchun Bian, Heng Lyu, Song Miao, Yunmei Li, Huaiqing Liu, and Jie Xu

***Abstract*—The particulate backscattering coefficient (b_{bp}) plays an important role in the underwater light field. However, it is difficult to accurately estimate $b_{\mathrm{bp}}(\lambda)$ in turbid inland water with complex optical properties. To accurately estimate the backscattering coefficients in inland water, a simple classification method based on the shape of remote sensing reflectance was first proposed to distinguish two water types (i.e., water type 1 and water type 2) with different backscattering characteristics. Then, trigonometric functions were developed to simulate the backscattering coefficients at all bands in water type 1 and the backscattering coefficients in the visible band of water type 2, whereas a linear function was built to estimate the backscattering coefficients in the near-infrared band of water type 2. The proposed algorithm was compared with four state-of-the-art methods and validated by an independently measured dataset of three lakes in the middle and lower reaches of the Yangtze River in 2020. The results showed that the proposed algorithm performed well in inland waters, with all mean absolute percentage errors $< 40\%$ and root-mean-square errors $< 0.25\ \mathrm{m}^{-1}$. Finally, the algorithm was applied to Ocean and Land Color Instrument images from 2016 to 2020 in Lake Taihu and Lake Hongze. It was found that the backscattering coefficients in Lake Taihu and Lake Hongze showed opposite seasonal variation trends, and the $b_{\mathrm{bp}}(676)$ in Lake Hongze began to decrease since 2017, whereas no obvious interannual variation was observed in Taihu Lake in recent five years.**

***Index Terms*—Estimation algorithms, inland waters, ocean and land color instrument (OLCI) images, particulate backscattering coefficient.**

I. Introduction

As one of the most important inherent optical properties (IOPs), the particulate backscattering coefficient (b_{bp}) is determined by particle features, such as concentration, size, shape, and composition, and plays a critical role in the backscattering of light from a water body to the sky received by satellite sensors [1], [2]. Therefore, particulate backscattering properties could provide important particle information that can be captured through remote sensing. Recently, $b_{\mathrm{bp}}(\lambda)$ has been widely used to indicate some important parameters representing water quality and biochemical characteristics, such as total suspended matter (TSM), particulate organic carbon (POC), and particle size [3]–[5]. As a result, understanding the particulate backscattering characteristics can further grasp the horizontal transport of suspended particulate matter (SPM), as well as the characteristics of vertical flocculation, sedimentation, resuspension, and siltation [6].

Recently, particulate backscattering characteristics in the ocean have been intensively studied. Studies have shown that the particulate backscattering coefficient in waters shows a downward trend, and the power-law function can be used to parameterize the backscattering coefficient [7]. In Gordon's research conducted in San Diego and Hawaii [8], it was found that the variation of particulate backscattering coefficients with wavelength dependence can be expressed by a power-law function. Rehm and Mobley [9] also found that estimated particulate backscattering coefficients based on upwelling radiance and downwelling irradiance decreased as the power-law function increased with wavelength. However, the particulate backscattering properties in inland waters may be different from those in the open ocean. Wu *et al.* [10] found that the particulate backscattering coefficient at 420 nm was lower than that at 440 nm in Lake Poyang, which was believed that the change did not follow the monotonic power function. It was also found in the VIIRS2014 dataset [11] that there was a peak in the particulate backscattering spectra at 442 and 530 nm and a drop at approximately 480 nm. Furthermore, our field particulate backscattering data collected in different turbid lakes did not show a power-law function of variation of particulate backscattering as the wavelength changed.

The accurate estimation of $b_{\mathrm{bp}}(\lambda)$ is essential for obtaining water biochemical features via remote sensing technology [12], [13]. In recent years, based on the quasi-analytical algorithm (QAA) [14], a series of remote sensing algorithms for estimating the IOPs of ocean, coastal and inland waters have been developed [15]–[17]. In the development of the algorithms,

Manuscript received May 10, 2021; revised July 6, 2021 and July 27, 2021; accepted August 12, 2021. Date of publication August 19, 2021; date of current version September 9, 2021. This work was supported in part by the National Natural Science Foundation of China under Grant 41871234 and in part by the Postgraduate Research and Practice Innovation Program of Jiangsu Province, China under Grant KYCX20_1177. *(Corresponding author: Heng Lyu.)*

Jiafeng Xu, Yingchun Bian, Song Miao, Huaiqing Liu, and Jie Xu are with the Key Laboratory of Virtual Geographic Environment of Education Ministry, Nanjing Normal University, Nanjing 210023, China (e-mail: 201301036@njnu.edu.cn; 1834592815@qq.com; njnums1214@163.com; 1778041070@qq.com; 171301036@stu.njnu.edu.cn).

Heng Lyu and Yunmei Li are with the Key Laboratory of Virtual Geographic Environment of Education Ministry, Nanjing Normal University, Nanjing 210023, China, and also with the Jiangsu Center for Collaboration Invocation in Geographical Information Resource Development and Application, Nanjing 210023, China (e-mail: heng.lyu@gmail.com; liyunmei@njnu.edu.cn).

Digital Object Identifier 10.1109/JSTARS.2021.3106262

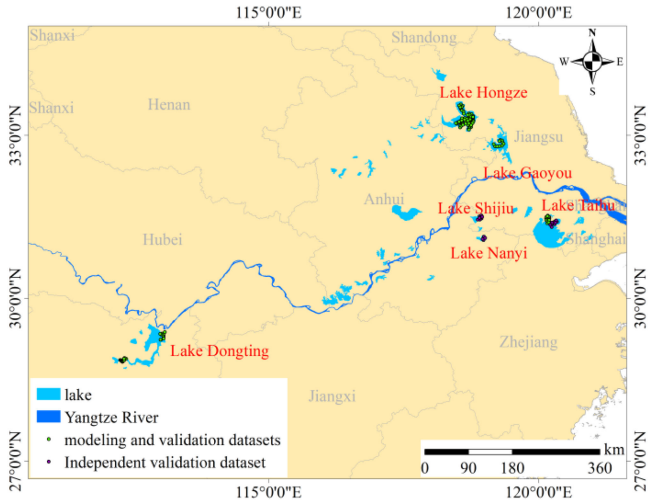

Fig. 1. Spatial distribution of sampling sites in turbid inland lakes from 2015 to 2018. The sampling points shown in green were collected from Lake Hongze, Lake Dongting, Lake Gaoyou, and Meiliang Bay of Lake Taihu, which were used for modeling and validation. The sampling points shown in deep red were collected from Lake Shijiu, Lake Nanyi, and Gonghu Bay of Lake Taihu, which were used for the independent validation dataset.

it was assumed that particulate backscattering variation with wavelength changes follows the power-law function. Then, according to different water optical characteristics, modifying the reference band of the backscattering coefficient was often adopted to improve the backscattering coefficient estimation accuracy, such as moving the reference band to the longer wave direction in turbid waters [18]. However, it has been found that the measured backscattering spectrum in inland water is very different from the power function [10], [11], thus, whether QAA-based estimation method can be applied to inland turbid water needs to be further investigated. As a result, there is an urgent need to develop a practical method to estimate the particulate backscattering coefficient and to propose a function to describe the relationship between $b_{\rm bp}(\lambda)$ and wavelength for inland water.

It is still a challenge to estimate $b_{\rm bp}(\lambda)$ in inland turbid lakes. Therefore, based on the field campaigns in typical turbid inland waters (Lake Taihu, Lake Hongze, Lake Dongting, and Lake Gaoyou in China), the purposes of this study were to 1) explore the varying characteristics of $b_{\rm bp}$ as the wavelength changes in turbid inland water and 2) develop an estimation algorithm of $b_{\rm bp}(\lambda)$ suitable for turbid inland water based on Ocean and Land Color Instrument (OLCI) images.

II. Data and Methods

A. Field Sampling and Measurement

A total of 120 samples that were collected through seven cruises from 2015 to 2018 were utilized to develop an estimation model for backscattering coefficients. The spatial distribution of sampling sites is shown in Fig. 1. In detail, 70 samples were collected during four cruises in Lake Hongze, 14 samples during one cruise in Meiliang Bay of Lake Taihu, ten samples during one cruise in Lake Gaoyou, and 26 samples during one cruise in Lake Dongting. For validating the backscattering retrievals, an independent database ($N = 21$) collected from Gonghu Bay of Lake Taihu, Lake Nanyi, and Lake Shijiu was applied. Furthermore, a database ($N = 28$) collected from the Chesapeake Bay obtained from SeaBASS [19] was also used to evaluate the applicability of the developed algorithm.

Remote sensing reflectance ($R_{\rm rs}(\lambda)$), particulate backscattering coefficients ($b_{\rm bp}(\lambda)$), and particle size distribution of suspended particles were collected at each sampling point. In brief, $R_{\rm rs}(\lambda)$ was obtained by a FieldSpec spectroradiometer [20]. Particulate backscattering coefficients in six bands (442, 488, 532, 590, 676, and 852 nm) were measured by using a HOBI Labs Hydroscat-6P (HS-6P) [21]. Before cruising, HS-6 was calibrated to confirm its performance. The sigma correction was performed on the measurement data under the guidance of the HOBI Labs user manual. The specific correction formula is as follows:

$$b_b = \sigma b_{\rm bu} \tag{1}$$

where b_b is the corrected backscattering coefficient, $b_{\rm bu}$ is the measured backscattering coefficient without sigma correction, and σ is the correction coefficient and its calculation method is shown in the following equation:

$$\sigma = k_1 \exp\left(k_{\rm exp} k_{\rm bb}\right) \tag{2}$$

where k_1 is equal to 1 at all wavelength, $k_{\rm exp}$ is a parameter related to the instrument and included in calibration file, and $k_{\rm bb}$ is the attenuation of the backscattering signal.

Data correction is the energy compensation for the attenuation of the optical signal in the entire optical path transmission, and the relationship shown in (3) was used to compensate for the attenuation [22]

$$k_{\rm bb} = a + 0.4b \tag{3}$$

where a is the total absorption coefficient and b is the scattering coefficient. b was calculated based on the backscattering probability $\widetilde{b_b}$, as shown in in the following equation:

$$b = (b_{\rm bu} - b_{\rm bw})/\widetilde{b_b} \tag{4}$$

where $\widetilde{b_b}$ was considered to be 0.019 [23], and $b_{\rm bw}$ is the backscattering coefficient of pure water.

Finally, by subtracting the $b_{\rm bw}$ from the corrected backscattering coefficient b_b, the particulate backscattering coefficient $b_{\rm bp}$ was obtained

$$b_{\rm bp} = b_b - b_{\rm bw}. \tag{5}$$

The particulate backscattering coefficients at 488 nm of the 24 sampling points could not be used due to negative values caused by noise, so only 96 sampling points were applied to develop an algorithm for estimating particulate backscattering coefficient at 488 nm. The particle size volume concentration (V (D), μL•L-1) was measured by using a Sequoia LISST-100X. The median particle diameter of the volume distribution (D_v50, μm) was derived using the LISST-100X measurements [24].

Surface water (<0.5 m) was also taken at each sampling site with 2 L Niskin bottles for analysis. Chlorophyll-a (Chla) was

extracted with 90% ethanol. The concentrations of TSM, organic suspended matter, and inorganic suspended matter (ISM) were determined using the standard method [25]. The absorption of total particulate matter ($a_{\mathrm{p}}(\lambda)$), phytoplankton ($a_{\mathrm{ph}}(\lambda)$), and nonalgal particulate matter ($a_{\mathrm{nap}}(\lambda)$) was determined by using the transmittance–reflectance technique with a Shimadzu UV2550 spectrophotometer [26].

B. Accuracy Assessment

The coefficient of determination (R^2), mean absolute percentage error (MAPE), and root-mean-square error (RMSE) were used to quantitatively evaluate the performance of the particulate backscattering coefficient estimation model

$$R^2 = 1 - \sum_{i=1}^{n} (X_i - Y_i) \Big/ \sum_{i=1}^{n} (X_i - Z) \tag{6}$$

$$\mathrm{MAPE} = \frac{1}{n} \sum_{i=1}^{n} \left| \frac{X_i - Y_i}{Y_i} \right| \times 100\% \tag{7}$$

$$\mathrm{RMSE} = \sqrt{\frac{1}{n} \sum\nolimits_{i=1}^{n} (X_i - Y_i)^2} \tag{8}$$

where X_i and Y_i are the values of *in situ* measurement and estimation from remote sensing reflectance, respectively, and Z is the mean value of the *in situ* measured dataset.

C. Sentinel-3A/OLCI Image Preprocessing

With a spatial resolution of 300 m, a total of 21 bands, and a high signal-to-noise ratio, Sentinel-3A/OLCI is an effective ocean color sensor for monitoring water quality in inland water. A total of 257 images (68 images for Lake Taihu, 189 images for Lake Hongze) from June 2016 to May 2020 were downloaded from the European Space Agency Copernicus Open Access Hub. Three often used methods for atmospheric correction in inland turbid waters, Case 2 Regional Coast Color processor (C2RCC), and the management unit of the North Seas Mathematical Models (MUMM) [27] and Dense dark vegetation Water area correction (DW) [28] were extensively compared. The parameters of C2RCC were set as salinity = 35.0 PSU, temperature = 15.0 °C, ozone = 330.0 DU, air pressure = 1000.0 hPa. The MUMM_alpha and MUMM_gamma of MUMM atmospheric correction were set to 1.817 and 1, respectively [29]–[31]. The remote sensing reflectance of 45 quasi-synchronous points with acquired OLCI images from July 22, 2016, December 7, 2017, May 18, 2017, September 8-9, 2019 were used to validate the accuracy of atmospheric correction. The scatterplot of measured remote sensing reflectance and atmospheric corrected remote sensing reflectance derived from OLCI images is illustrated in Fig. 2 and the statistics are listed in Table I. And it can be seen that the performance of C2RCC was the worst, and the corrected remote sensing reflectance was significantly overestimated. The performance of the DW algorithm in the visible band was slightly better than the MUMM algorithm, but in the near-infrared band, the consistency between the remote sensing reflectance estimated by the DW algorithm and the measured remote sensing reflectance was poor. Compared with the other two algorithms, the MUMM algorithm was more stable in the visible bands and the near-infrared bands. Therefore, the MUMM algorithm was finally adopted to conduct atmospheric correction for OLCI images.

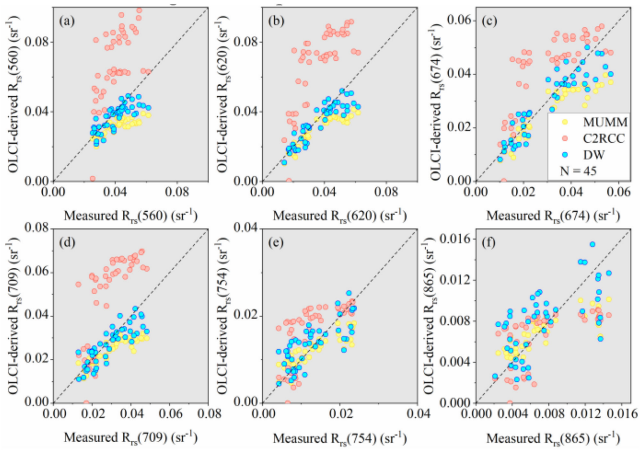

Fig. 2. Scatterplot of the field-measured remote sensing reflectance and OLCI-derived remote sensing reflectance using MUMM and C2RCC atmospheric correction models at (a) 560 nm, (b) 620 nm, (c) 674 nm, (d) 709 nm, (e) 754 nm, and (f) 865 nm.

Algal bloom areas were masked using VB-FAH [32]. If the value of the index was greater than 0.0039, a pixel was considered an algal bloom pixel.

III. Algorithm Development

First, to accurately estimate particulate backscattering coefficients in inland water with complex optical characteristics, the water type must be determined based on optical characteristics. This was achieved with a classification method based on the remote sensing reflectance spectrum and the detailed determination method is shown in (9). Specifically, the ratio of $R_{\mathrm{rs}}(560)/R_{\mathrm{rs}}(620)$ and the value of $R_{\mathrm{rs}}(754)$ were proposed to classify the water types as follows:

$$\begin{cases} \dfrac{R_{\mathrm{rs}}(560)}{R_{\mathrm{rs}}(620)} \le 1 \; or \; R_{\mathrm{rs}}(754) \ge 0.019 \; \mathrm{sr}^{-1} \; Water \; type \; 1 \\ \dfrac{R_{\mathrm{rs}}(560)}{R_{\mathrm{rs}}(620)} > 1 \; and \; R_{\mathrm{rs}}(754) < 0.019 \; \mathrm{sr}^{-1} \; Water \; type \; 2 \end{cases} \tag{9}$$

where $R_{\mathrm{rs}}(560)$, $R_{\mathrm{rs}}(620)$, and $R_{\mathrm{rs}}(754)$ are the remote sensing reflectance at 560, 620, and 754 nm, respectively.

When $R_{\mathrm{rs}}(560)/R_{\mathrm{rs}}(620)$ was greater than 1 and $R_{\mathrm{rs}}(754)$ was less than 0.019 sr^{-1}, the measurement was defined as water type 2 with low to moderate TSM (29.38±14.82 mg/L). Otherwise, the measurement was considered as water type 1 with very high TSM (77.62±29.21 mg/L). Based on the above classification method, 42 sampling points were classified as water type 1, and the remaining 78 samples were classified as water type 2. Two-third of the field samples in each water type were used as the modeling dataset, and the remaining one-third of the field samples were used as the validation dataset. The sampling number of backscattering coefficients is listed in Table II.

The measured backscattering spectra of the two water types are shown in Fig. 3. The particulate backscattering in turbid

TABLE I
STATISTICS OF THE ACCURACY OF MUMM, C2RCC, AND DW AT 560, 620, 674, 709, 754, AND 865 NM

method	statistics	$R_{rs}(560)$	$R_{rs}(620)$	$R_{rs}(674)$	$R_{rs}(709)$	$R_{rs}(754)$	$R_{rs}(865)$
C2RCC	R^2	0.40	0.59	0.59	0.53	0.43	0.35
	MAPE (%)	72.60	95.16	51.81	84.47	57.93	43.11
	RMSE (sr^{-1})	0.031	0.034	0.015	0.026	0.026	0.003
MUMM	R^2	0.55	0.83	0.86	0.76	0.66	0.55
	MAPE (%)	22.27	20.52	19.47	22.02	24.54	26.35
	RMSE (sr^{-1})	0.012	0.010	0.009	0.009	0.004	0.003
DW	R^2	0.61	0.82	0.84	0.72	0.58	0.42
	MAPE (%)	12.39	13.07	14.68	16.56	33.05	42.98
	RMSE (sr^{-1})	0.007	0.006	0.006	0.006	0.004	0.003

TABLE II
NUMBER OF BACKSCATTERING COEFFICIENTS AT 442, 488, 532, 590, 676, 852 NM

Number	442 nm	488 nm	532 nm	590 nm	676 nm	852 nm
Water type 1 development dataset	28	26	28	28	28	28
Water type 1 validation dataset	14	12	14	14	14	14
Water type 2 development dataset	52	35	52	52	52	52
Water type 2 validation dataset	26	23	26	26	26	26
Total number	120	96	120	120	120	120

inland water does not decay continuously in the form of a power-law function in inland turbid water. It can be seen that in Fig. 3, for both water type 1 and water type 2, the particulate backscattering value was low in the blue bands (442 and 488 nm), followed by the highest particulate backscattering coefficient at 590 nm, then a relatively low value in the red band (676 nm). Therefore, given these observations, the variation within the visible band can be approximately simulated by using the trigonometric function.

A trigonometric function described by (10) was developed to describe the particulate backscattering variation as the wavelength changes in the range of 442–852 nm for water type 1

$$b_{\mathrm{bp}}\ (\lambda) = A_{\mathrm{type1}}\ \cos\left(W_{\mathrm{type1}}\left(\lambda - 852\right)\right) + b_{\mathrm{bp}}\left(852\right) - A_{\mathrm{type1}} \tag{10}$$

where A_{type1} is the coefficient of the trigonometric function for water type 1, which represents the amplitude of the trigonometric function. The parameter A_{type1} in (10) for water type 1 was derived based on particulate backscattering at 852 and 488 nm using (11). W_{type1} was calculated from the difference between the wavelength of 852 and 488 nm using (12), the peak and drop values of the backscattering spectrum. Here, W_{type1} was a parameter describing the period of a trigonometric function. $b_{\mathrm{bp}}(852)$ is the particulate backscattering coefficient at 852 nm

$$A_{\mathrm{type1}} = \frac{b_{\mathrm{bp}}\left(852\right) - b_{\mathrm{bp}}\left(488\right)}{2} \tag{11}$$

where $b_{\mathrm{bp}}(488)$ and $b_{\mathrm{bp}}(852)$ are the particulate backscattering coefficients at 488 and 852 nm, respectively.

The backscattering spectrum of water type 1 can be approximately regarded as a trigonometric function with a minimum value at 488 nm and a maximum value at 852 nm so that W_{type1} can be calculated based on the period of the trigonometric function using the following equation:

$$W_{\mathrm{type1}} = \frac{2\pi}{T_{\mathrm{type1}}} = \frac{2\pi}{\frac{2}{3} \times (852 - 488)} \tag{12}$$

where T_{type1} is the period of the trigonometric function of water type 1.

Since water type 1 belongs to high TSM concentration water, the saturation phenomenon of remote sensing reflectance in visible bands was often observed; as a result, the particulate backscattering variation was more sensitive to reflectance in near-infrared bands, and it was found that A_{type1} had the highest correlation with $R_{\mathrm{rs}}(754)/R_{\mathrm{rs}}(560)$. Thus, A_{type1} could be derived by using $R_{\mathrm{rs}}(754)/R_{\mathrm{rs}}(560)$, as shown in (13), and the relationship between A_{type1} and $R_{\mathrm{rs}}(754)/R_{\mathrm{rs}}(560)$ is illustrated in Fig. 4(a)

$$A_{\mathrm{type1}} = 2.7606\left(\frac{R_{\mathrm{rs}}\left(754\right)}{R_{\mathrm{rs}}\left(560\right)}\right)^{2.8252}, \quad R^2 = 0.72 \tag{13}$$

where $R_{\mathrm{rs}}(560)$ and $R_{\mathrm{rs}}(754)$ are the remote sensing reflectance at 560 and 754 nm, respectively.

However, in water type 2, in the near-infrared bands, the particulate backscattering coefficient did not change much or even showed a slight decrease. Therefore, the piecewise function method was proposed to simulate the particulate backscattering coefficient variation as the wavelength changes. In the wavelength range of 442–676 nm, a trigonometric function was built to simulate particulate backscattering coefficient variation, defined as shown in (14). In the wavelength range from 676 to 852 nm, a linear function was developed to describe the particulate backscattering coefficient change in this range, as

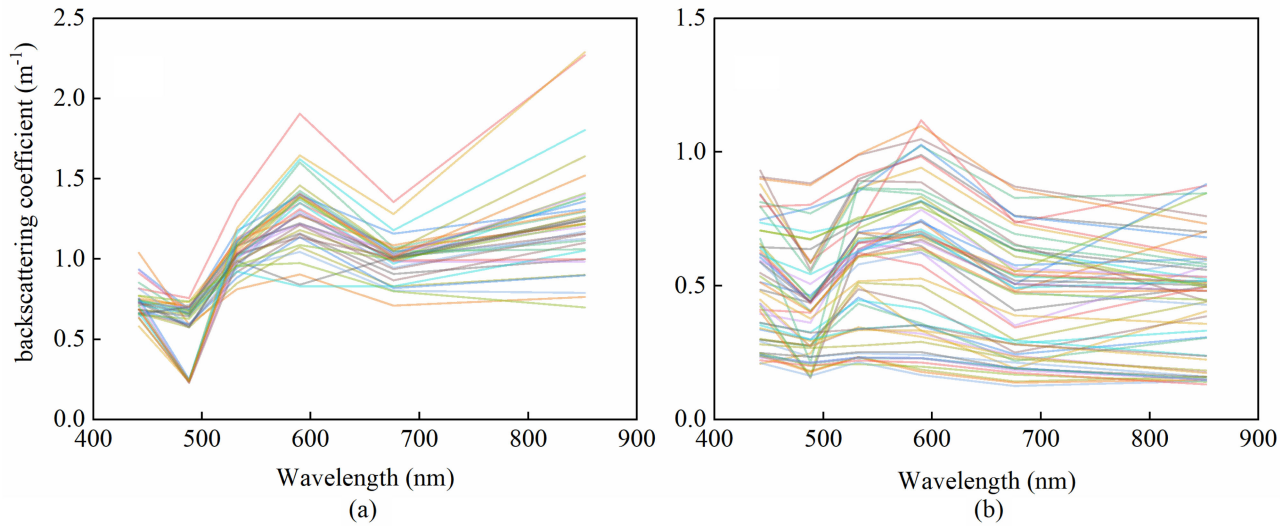

Fig. 3. (a) Measured backscattering of water type 1. (b) Measured backscattering of water type 2.

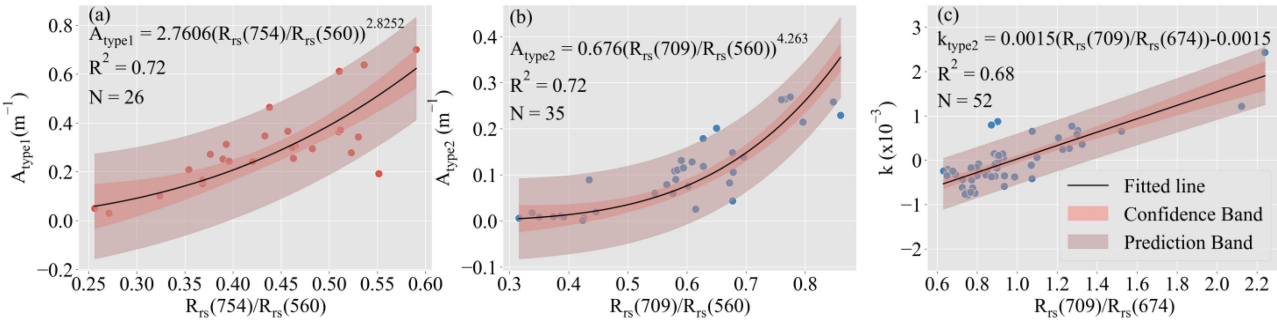

Fig. 4. Relationship between (a) *in situ* measured A_{type1} and $R_{\mathrm{rs}}(754)/R_{\mathrm{rs}}(560)$, (b) *in situ* measured A_{type2} and $R_{\mathrm{rs}}(709)/R_{\mathrm{rs}}(560)$, and (c) *in situ* measured k and $R_{\mathrm{rs}}(709)/R_{\mathrm{rs}}(674)$. The *in situ* measured A_{type1}, A_{type2}, and k were calculated from measured backscattering coefficients given in (13), (19), and (20). The number of *in situ* samples for A_{type1} and A_{type2} excluded the samples with signal noise at 488 nm.

shown in (15)

$$b_{\mathrm{bp}}(\lambda) = A_{\mathrm{type2}} \cos\left(W_{\mathrm{type2}}(\lambda - 590)\right) + b_{\mathrm{bp}}(676) - A_{\mathrm{type2}} \cos\left(W_{\mathrm{type2}}(676 - 590)\right),\ \lambda \le 676\ \mathrm{nm} \tag{14}$$

$$b_{\mathrm{bp}}(\lambda) = k(\lambda - 852) + b_{\mathrm{bp}}(852),\ 676\ \mathrm{nm} \le \lambda \le 852\ \mathrm{nm} \tag{15}$$

where A_{type2} is the coefficient of the trigonometric function for water type 2, which represents the amplitude of the trigonometric function. Parameter A_{type2} in (14) for water type 2 was derived based on particulate backscattering at 590 and 488 nm using (16), the peak and dip values of the backscattering spectrum. W_{type2} was calculated from the difference between the wavelength of 590 and 488 nm using (17). Here, W_{type2} was a parameter describing the period of a trigonometric function. k is the slope of the linear function for water type 2 defined as (18), and $b_{\mathrm{bp}}(852)$ is the particulate backscattering coefficient at 852 nm

$$A_{\mathrm{type2}} = \frac{b_{\mathrm{bp}}(590) - b_{\mathrm{bp}}(488)}{2} \tag{16}$$

where $b_{\mathrm{bp}}(488)$ and $b_{\mathrm{bp}}(590)$ are the particulate backscattering coefficients at 488 and 590 nm, respectively.

The backscattering spectrum of water type 2 can be approximately regarded as a trigonometric function with a minimum value at 488 nm and a maximum value at 590 nm so that W_{type2} can be calculated based on the period of the trigonometric function using the following equation:

$$W_{\mathrm{type2}} = \frac{2\pi}{T_{\mathrm{type2}}} = \frac{2\pi}{2 \times (590 - 488)} \tag{17}$$

where T_{type2} is the period of the trigonometric function of water type 2.

The parameter k, the slope of the linear function for water type 2, was calculated using the following equation:

$$k = \frac{b_{\mathrm{bp}}(852) - b_{\mathrm{bp}}(676)}{852 - 676} \tag{18}$$

where $b_{\mathrm{bp}}(676)$ and $b_{\mathrm{bp}}(852)$ are the particulate backscattering coefficients at 676 and 852 nm, respectively.

Since water type 2 was not high TSM concentration water, the remote sensing reflectance at short wavelengths does not show saturation [33]–[35]. It was found that A_{type2} was affected by

particles and had a significant correlation with the reflectance at short wavelengths. Therefore, the ratio of $R_{rs}(709)/R_{rs}(560)$ was adopted to calculate A_{type2}, as shown in (19), due to its significant positive correlation with A_{type2} ($r = 0.87$, $p < 0.05$). Their relationship is shown in Fig. 4(b)

$$A_{type2} = 0.676\left(\frac{R_{rs}(709)}{R_{rs}(560)}\right)^{4.263}, \quad R^2 = 0.72 \tag{19}$$

where $R_{rs}(560)$ and $R_{rs}(709)$ are the remote sensing reflectance at 560 and 709 nm, respectively.

In this study, k was found to present a significant positive correlation with the ratio of $R_{rs}(709)/R_{rs}(674)$ ($r = 0.83$, $p < 0.05$). This relationship is shown in Fig. 4(c). As a result, a linear regression was developed to estimate k using the ratio of $R_{rs}(709)/R_{rs}(674)$, as shown in the following equation:

$$k = 0.0015\frac{R_{rs}(709)}{R_{rs}(674)} - 0.0015, \quad R^2 = 0.68 \tag{20}$$

where $R_{rs}(674)$ and $R_{rs}(709)$ are the remote sensing reflectance at 674 and 709 nm, respectively.

The particulate backscattering coefficient at 852 nm was used as the initial reference value for estimation of the particulate backscattering coefficients in other bands, because particulate backscattering at 852 nm may be estimated using a semianalytical method due to the strong absorption of pure water in near-IR bands. Based on the assumptions that the total absorption at 852 nm can be regarded as the absorption of pure water [36], [17] and that the particulate backscattering at 852 nm is approximately equal to the particulate backscattering at 865 nm, the method proposed by Lyu *et al.* [37] was adopted to estimate the particulate backscattering coefficient at 852 nm by using the relationship between remote sensing reflectance and IOPs [14], [38]. The estimation algorithm is given in the following equation:

$$b_{bp}(852) \approx b_{bp}(865) = \frac{a_w(865) \times R_{rs}(865)}{0.0448 - R_{rs}(865)} - b_w(865) \tag{21}$$

where $a_w(865)$ and $b_w(865)$ are the pure water absorption and particulate backscattering coefficients, respectively. The values of $a_w(865)$ and $b_w(865)$ are 4.6052 and 0.00014 m^{-1}, respectively [39].

Finally, the particulate backscattering in all six bands can be obtained based on the reference particulate backscattering coefficients at a wavelength of 852 nm using (21) and the particulate backscattering coefficient simulation function using (10), (14), and (15). The procedures of backscattering coefficients estimation at six bands are shown in Fig. 5. And detailed estimation method and the purpose of each parameter used in the algorithm were listed in Table III.

IV. Result

A. Estimation Accuracy of Parameters of A and k

A and k are important parameters in the particulate backscattering coefficients simulation algorithm, therefore, the measured A and k values calculated using measured particulate backscattering coefficients and the estimated A and k values derived from remote sensing reflectance were employed to evaluate the estimation accuracy. The estimation performance of A_{type1} was satisfactory with a MAPE of 26.88%, an RMSE of 0.10 m^{-1}, and an R^2 of 0.89, and the scatterplot of estimated A_{type1} and measured A_{type1} is shown in Fig. 6(a). It can be seen that measured A_{type1} and estimated A_{type1} showed a good agreement, with a significant linear relationship ($r = 0.94$, $p < 0.05$, slope = 0.77). Similarly, the scatterplots of measured A_{type2} and k and estimated A_{type2} and k (Fig. 6(b) and (c), respectively) show that points were tightly distributed near the 1:1 line, with MAPE of 49.74% and 70.20%, RMSE of 0.04 and 0.0004 m^{-1}, and R^2 of 0.82 and 0.79, respectively. The higher MAPE was mainly caused by the fact that the *in situ* measured value was extremely small. Although the MAPE of the k value estimation was larger, there was little effect on the final estimation result of particulate backscattering coefficients. A significant strong correlation between estimated k and A_{type2} and *in situ* measured k ($r = 0.89$, $p < 0.05$) and A_{type2} ($r = 0.91$, $p < 0.05$) was found, suggesting that the estimation of k and A_{type2} through remote sensing is feasible.

According to the evaluation results, it can be concluded that the parameters of A_{type1} for water type 1 and k and A_{type2} for water type 2 water could be successfully obtained through remote sensing reflectance. Therefore, the obtained coefficients could be further used to estimate the particulate backscattering coefficients.

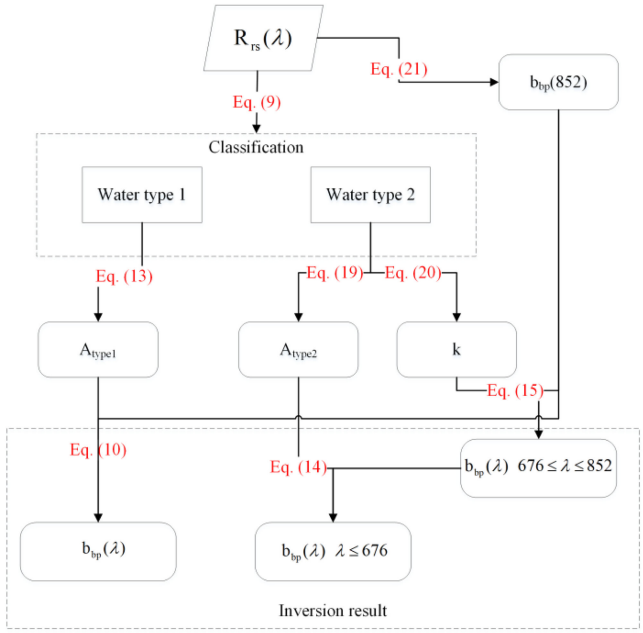

Fig. 5. Flowchart of the algorithm. Input parameters are remote sensing reflectance ($R_{rs}(\lambda)$). A_{type1}, A_{type2}, and k are coefficients of the backscattering inversion algorithm derived in (13), (19), and (20). Output variables are backscattering coefficients ($b_{bp}(\lambda)$).

B. Algorithm Performance Evaluation Based on in Situ Data

The remaining one-third of the field samples were used to validate the accuracy of the proposed algorithm. First, the *in situ* measured data were used to validate the estimation accuracy

TABLE III
DETAILED INTRODUCTION OF PARAMETERS USED IN THE ESTIMATION ALGORITHMS

Parameters	The purpose	Definition	Estimating method
A_{type1}	The amplitude of trigonometric function in water type 1	$A_{type1} = \frac{b_{bp}(852) - b_{bp}(488)}{2}$	$A_{type1} = 2.7606(\frac{R_{rs}(754)}{R_{rs}(560)})^{2.8252}$
A_{type2}	The amplitude of trigonometric function in water type 2	$A_{type1} = \frac{b_{bp}(590) - b_{bp}(488)}{2}$	$A_{type2} = 0.676(\frac{R_{rs}(709)}{R_{rs}(560)})^{4.263}$
k	The slope of linear function in water type 2	$k = \frac{b_{bp}(852) - b_{bp}(676)}{852 - 676}$	$k = 0.0015\frac{R_{rs}(709)}{R_{rs}(674)} - 0.0015$

$b_{bp}(488)$, $b_{bp}(590)$, $b_{bp}(676)$, and $b_{bp}(852)$ are the backscattering coefficient at 488, 590, 676, and 852 nm, respectively, and $R_{rs}(560)$, $R_{rs}(674)$, $R_{rs}(709)$, and $R_{rs}(754)$ are the remote sensing reflectance at 560, 674, 709, and 754 nm, respectively.

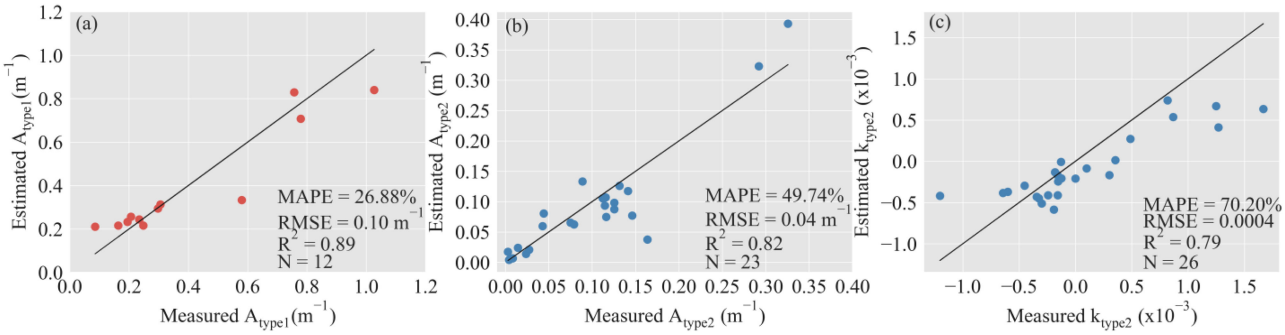

Fig. 6. Comparison of (a) *in situ* measured A_{type1} and estimated A_{type1} for the validation dataset of water type 1, (b) *in situ* measured A_{type2} and estimated A_{type2} for the validation dataset of water type 2, (c) *in situ* measured k and estimated k for the validation dataset of water type 2. The number of validation samples for A_{type1} and A_{type2} excluded the samples with signal noise at 488 nm.

of the particulate backscattering coefficient at 852 nm obtained by using the method proposed by Lyu *et al.* [37]. The scatter plot of the measured particulate backscattering coefficients and estimated values is shown in Fig. 7(f), and it can be seen that the estimated value was close to the measured value for both water type 1 and water type 2. The estimated $b_{bp}(852)$ and measured $b_{bp}(852)$ showed a strong agreement with a significant correlation of 0.92 ($p < 0.05$). The MAPE and RMSE of the estimation algorithm were further calculated, with values of 27.97% and 0.21 m^{-1}, respectively. Further analysis showed that the estimation accuracy of water type 1 was slightly better than water type 2. This result further demonstrated that the absorption of particles in both high and middle or low turbid water was so small compared with pure water in the near-infrared band [17], [40] that the influence of absorption of particles could be ignored without significantly affecting the particulate backscattering estimation values at 852 nm.

The estimated $b_{bp}(852)$, A_{type1}, A_{type2}, and k were then applied to simulate particulate backscattering coefficients in other bands for both types. The scattering plots of estimated values and measured values in six bands are shown in Fig. 7. The results showed that the algorithm has much better estimation accuracy at 590 nm with a relatively lower MAPE value of 25.56%, an RMSE value of 0.25 m^{-1} and an R^2 of 0.71. The estimation accuracy at 488 nm is slightly lower than for the other five bands, with a MAPE of 38.71%, an RMSE of 0.19 m^{-1} and an R^2 of 0.61. It was also found that there was an obvious overestimation phenomenon for water type 1. In summary, the evaluation results proved that the algorithm had acceptable performance in estimating the particulate backscattering coefficients in turbid inland water. Furthermore, the comparison between the measured backscattering spectrum and the estimated backscattering spectrum is shown in Fig. 8. It can be seen that, in general, the measured backscattering spectra of the two water types have a high consistency with the estimated results, with a correlation coefficient greater than 0.85. Although there are underestimations at 488 and 532 nm, the proposed algorithm can effectively reflect the high values of backscattering coefficients at 590 and 852 nm.

C. Comparison With Other Algorithms

Three often used methods, i.e., QAA-v6 [18], QAA-M14 [41], QAA-750E [17], which are based on the assumption that the backscattering spectrum following the power-law function, and Gons' method [40] were selected, to compare with the proposed algorithm. And the detailed estimation accuracy information of the four algorithms was listed in Table IV. Generally, it can be seen that the estimation accuracy of the proposed algorithm in this study is the highest with the lowest average MAPE and the minimum average RMSE among all algorithms. Specifically, the estimation accuracy of this proposed algorithm was slightly lower than that of QAA-v6 in the blue bands (442 and 488 nm),

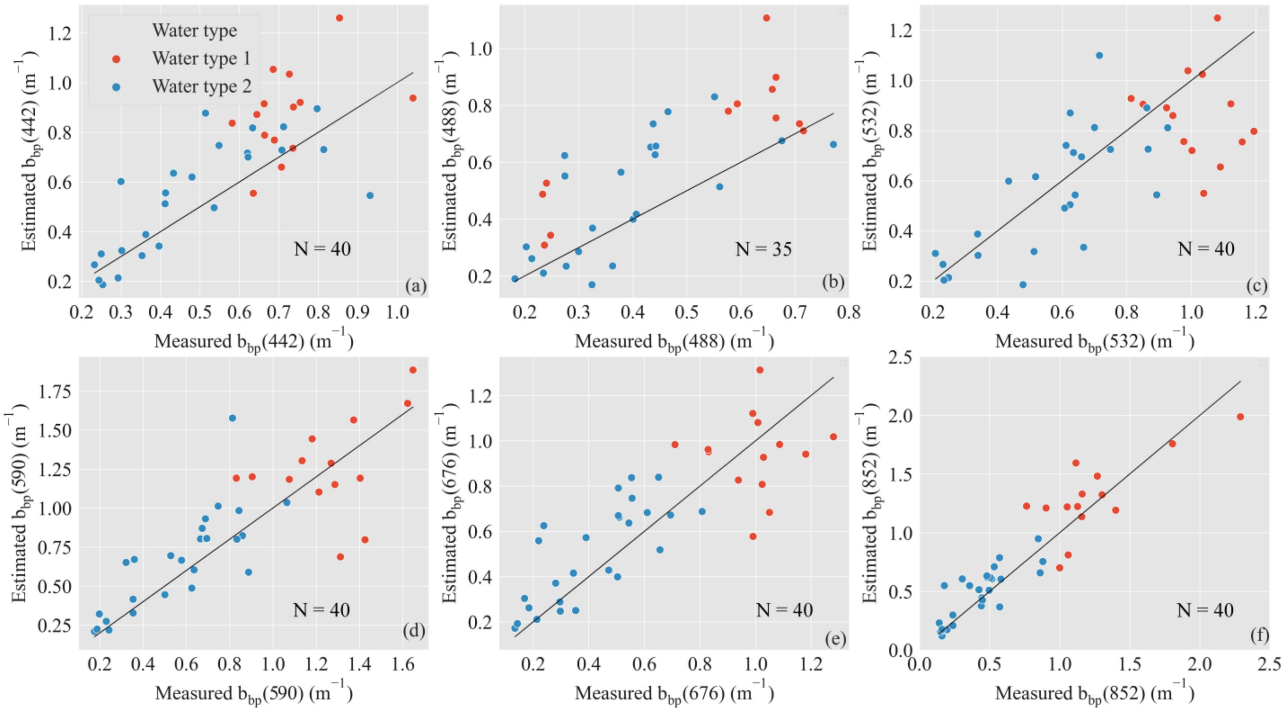

Fig. 7. Comparison of (a) *in situ* measured $b_{bp}(442)$ and estimated $b_{bp}(442)$, (b) *in situ* measured $b_{bp}(488)$ and estimated $b_{bp}(488)$, (c) *in situ* measured $b_{bp}(532)$ and estimated $b_{bp}(532)$, (d) *in situ* measured $b_{bp}(590)$ and estimated $b_{bp}(590)$, (e) *in situ* measured $b_{bp}(676)$ and estimated $b_{bp}(676)$, and (f) *in situ* measured $b_{bp}(852)$ and estimated $b_{bp}(852)$ for both water type 1 and water type 2.

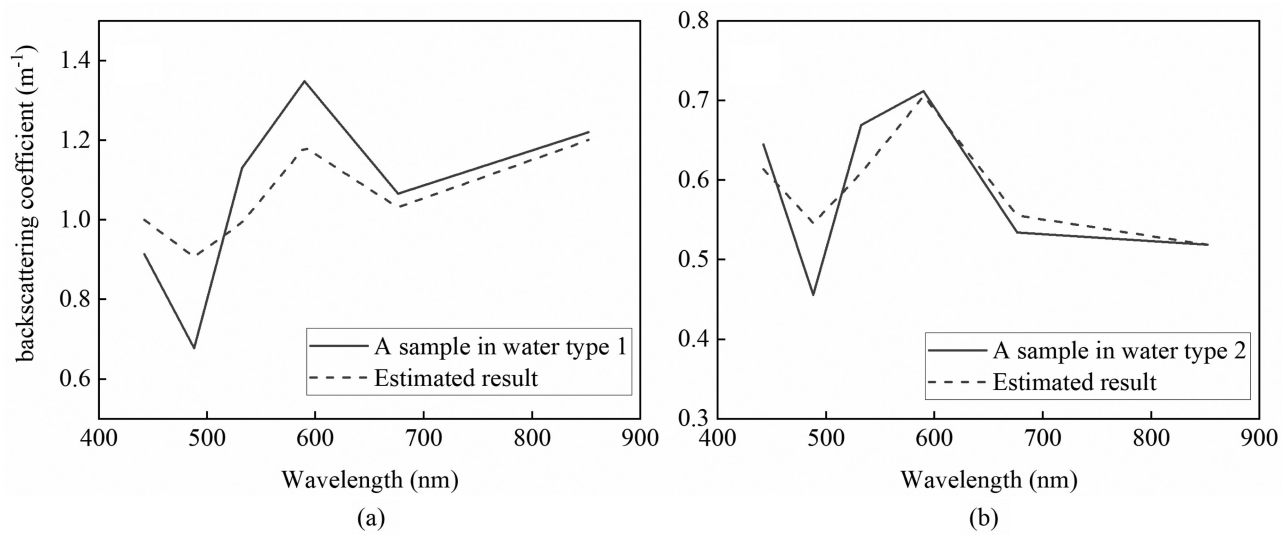

Fig. 8. Particulate backscattering spectral estimation result of a sample point in (a) water type 1 and the estimated result of a sample point in (b) water type 2.

but much better than QAA-M14. At 532 and 590 nm, the estimation performance of this proposed algorithm was significantly better than QAA-v6, especially at 532 and 590 nm, whereas was slightly lower than that of QAA-M14. At 852 nm, excluding Gons' method, the QAA-v6 has the worst estimation accuracy with the MAPE up to 39.14%, and this proposed algorithm has the best performance with the lowest RMSE. This was mainly because the monotonically decreasing power-law function could not express the enhancement of the backscattering coefficients in the red or near-infrared band. Compared with the proposed algorithm, QAA-v6 and QAA-M14, QAA-750E had a higher R^2, but there is a significant difference in magnitude between its estimated values and the measured values, with greater MAPE and RMSE. Besides, Gons [40] proposed an algorithm to estimate the backscattering coefficient for the near-infrared band, in which they think that the backscattering in the near-infrared band is wavelength-independent. Therefore, *in situ* measured $b_{bp}(852)$ was used to evaluate the estimation accuracy of $b_{bp}(776)$ derived based on Gons' algorithm. The comparison result showed that this proposed algorithm has much

TABLE IV
COMPARISON OF THE PROPOSED ALGORITHM IN THIS STUDY WITH QAA-V6, QAA-M14, QAA-750E, AND GONS' METHOD

Model		$b_{bp}(442)$	$b_{bp}(488)$	$b_{bp}(532)$	$b_{bp}(590)$	$b_{bp}(676)$	$b_{bp}(852)$	average
This study	R^2	0.60	0.61	0.54	0.71	0.64	0.85	0.66
	MAPE (%)	29.24	38.71	22.51	25.56	32.44	28.49	29.49
	RMSE (m^{-1})	0.21	0.19	0.21	0.25	0.21	0.21	0.21
QAA-v6	R^2	0.66	0.70	0.68	0.68	0.76	0.52	0.66
	MAPE (%)	27.95	43.04	27.51	34.02	24.87	39.14	32.76
	RMSE (m^{-1})	0.19	0.21	0.24	0.39	0.22	0.50	0.29
QAA-M14	R^2	0.51	0.53	0.76	0.78	0.82	0.73	0.69
	MAPE (%)	34.45	58.76	19.29	24.47	18.32	26.84	30.36
	RMSE (m^{-1})	0.27	0.28	0.18	0.32	0.16	0.43	0.27
QAA-750E	R^2	0.44	0.53	0.75	0.79	0.83	0.85	0.72
	MAPE (%)	234.23	262.09	91.94	49.49	55.90	22.18	119.31
	RMSE (m^{-1})	1.76	1.34	0.92	0.51	0.40	0.28	0.87
Gons' method	R^2	-	-	-	-	-	0.86	0.86
	MAPE (%)	-	-	-	-	-	58.13	58.13
	RMSE (m^{-1})	-	-	-	-	-	0.58	0.58

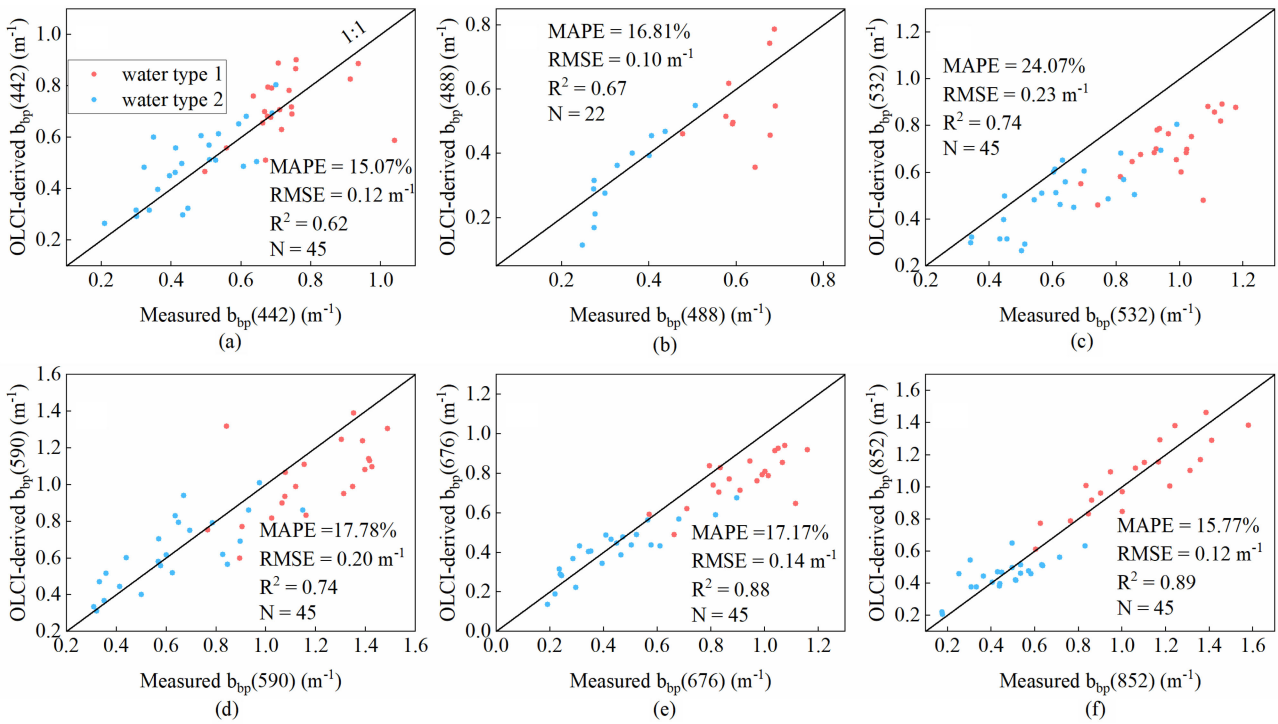

Fig. 9. Comparison of (a) *in situ* measured $b_{bp}(442)$ and OLCI-derived $b_{bp}(442)$, (b) *in situ* measured $b_{bp}(488)$ and OLCI-derived $b_{bp}(488)$, (c) *in situ* measured $b_{bp}(532)$ and OLCI-derived $b_{bp}(532)$, (d) *in situ* measured $b_{bp}(590)$ and OLCI-derived $b_{bp}(590)$, (e) *in situ* measured $b_{bp}(676)$ and OLCI-derived $b_{bp}(676)$, and (f) *in situ* measured $b_{bp}(852)$ and OLCI-derived $b_{bp}(852)$ for synchronous sampling points.

higher accuracy than that of Gons' algorithm with a MAPE of 58% in the near-infrared band in inland water. From our *in situ* measured data, it can be seen that the backscattering coefficient in the near-infrared band may vary obviously when the wavelength changes largely. The hypothesis about backscattering in the near-infrared band may no longer be valid for inland turbid water with high TSM concentration.

D. Spatiotemporal Variation Features of Particulate Backscattering Properties in Lake Hongze and Lake Taihu

The developed algorithm was employed to analyze the particulate backscattering spatiotemporal variation features in Lake Hongze and Lake Taihu using Sentinel-3A OLCI images as a demonstration of the algorithm's applicability. First, the OLCI images were atmospherically corrected using the MUMM method; 45 quasi-synchronous points with acquired OLCI images on July 22, 2016, December 7, 2017, May 18, 2017, September 8-9, 2019 were used to evaluate the performance of estimating backscattering coefficients using real OLCI images. In total, 22 quasi-synchronous points can be used to evaluate the estimation accuracy of the backscattering coefficient at 488 nm on OLCI images. The scatterplot of OLCI-derived particulate backscattering coefficients and measured particulate backscattering coefficients in the six bands is shown in Fig. 9. It was found that the estimation accuracy was acceptable with all MAPEs $<$ 24.07% and RMSEs $< 0.23\ m^{-1}$. No significant underestimation of the particulate backscattering coefficients was found, except

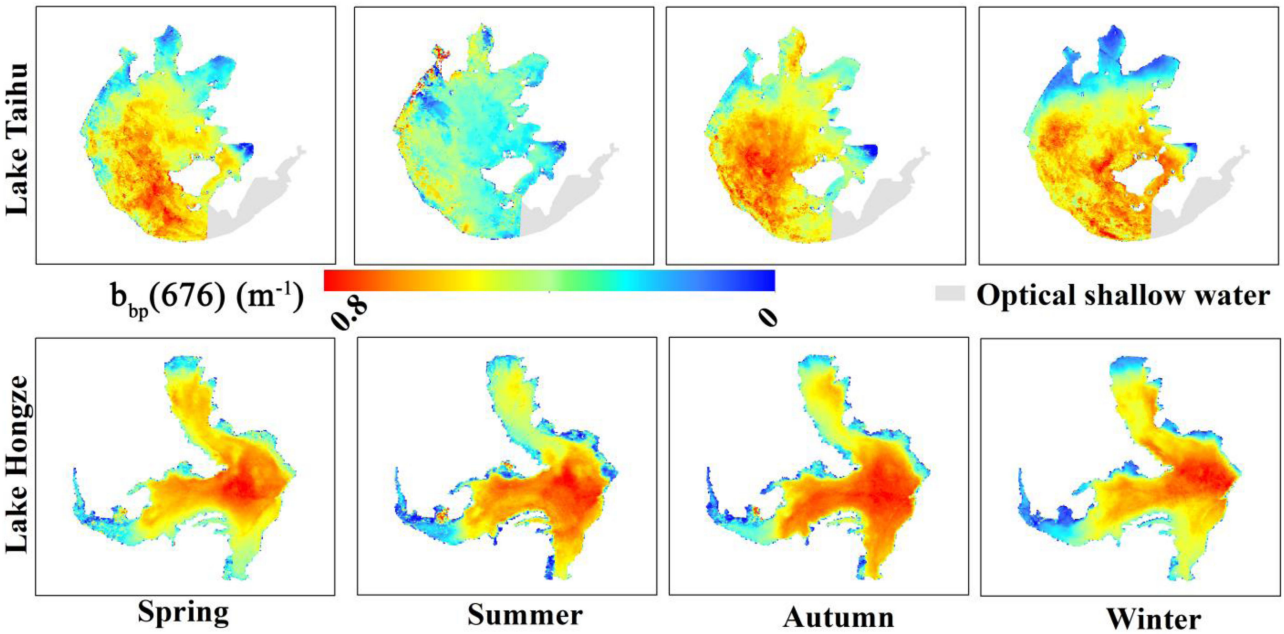

Fig. 10. OLCI-derived average $b_{bp}(676)$ for four seasons in Lake Taihu and Lake Hongze generated using the proposed model from June 2016 to May 2020.

for $b_{bp}(532)$. The evaluation result showed that the highest estimation accuracy is at 852 nm among all six bands, with a MAPE of 15.77%, an RMSE of 0.12 m^{-1} and an R^2 of 0.89, followed by is at 676 nm, with a MAPE of 17.17%, an RMSE of 0.14 m^{-1}, and an R^2 of 0.88. The poorest estimation accuracy is at 532 nm with a MAPE of 24.07%, an RMSE of 0.23 m^{-1}, and an R^2 of 0.74. It can be seen that the estimation accuracy using real OLCI images was acceptable and the developed algorithm can be applied to mapping the backscattering coefficients in Lake Taihu and Lake Hongze based on OLCI image.

Thus, the developed algorithm was applied to OLCI images from June 2016 to May 2020 to explore the temporal and spatial variation of $b_{bp}(676)$ in Lake Taihu and Lake Hongze because $b_{bp}(676)$ can be used as an indicator of particle composition information. All the images in each season are averaged to obtain the spatial distribution of the four seasons as shown in Fig. 10, and the effective pixels of all images in each month were averaged to obtain the mean value of each month as shown in Fig. 11. From 2016 to 2020, $b_{bp}(676)$ exhibited a distinct difference in spatial and temporal distributions in Lake Taihu and Lake Hongze. In Lake Taihu, $b_{bp}(676)$ was higher in the southwest and lower in the north, as shown in Fig. 10, which was consistent with the spatial distribution characteristics of TSM [12], [42], [43]. The inflow rivers mainly distributed in the west of Lake Taihu carry a large number of particles into the lake [44], which leads to the long-term higher $b_{bp}(676)$. At the same time, stronger wind in the west of Lake Taihu leads to more sediment resuspension [45], and more small inorganic particles result in higher $b_{bp}(676)$ than other regions. Spatially, it can be observed in Fig. 10 that $b_{bp}(676)$ of the southern and central regions was higher than that of the northern and western regions in Lake Hongze. The spatial distribution of $b_{bp}(676)$ in Lake Hongze was mainly affected by the discharge of input rivers, of which the Huaihe River accounts for 70% of the total

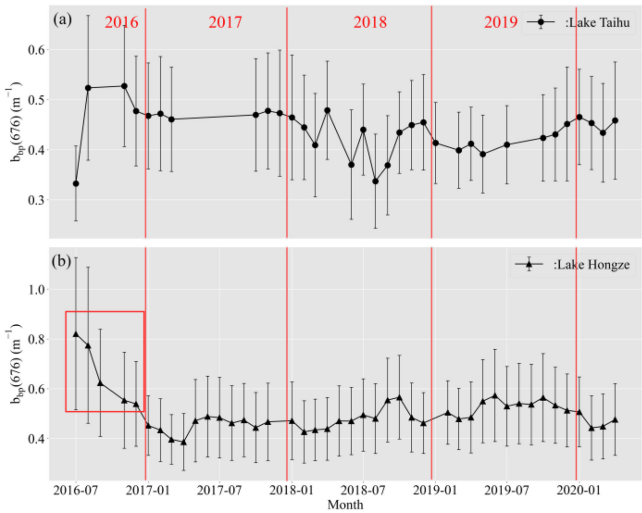

Fig. 11. Monthly variation in $b_{bp}(676)$ derived from OLCI in (a) Lake Taihu and (b) Lake Hongze from June 2016 to May 2020.

inflow [46]. Suspended sediment from the upper reaches of Huaihe River is carried into Lake Hongze [6], [47], which leads to higher $b_{bp}(676)$ in the nearby area.

Seasonal variation in $b_{bp}(676)$ in Lake Taihu and Lake Hongze is illustrated in Fig. 10. $b_{bp}(676)$ showed remarkable seasonal variation in both lakes, especially in Lake Taihu. Overall, $b_{bp}(676)$ in Lake Taihu was higher in spring (March–May) and winter (December–February) than in summer (June–August) and autumn (September–November). However, since Meiliang Bay and Zhushan Bay are dominated by phytoplankton, the significant increase of phytoplankton in summer and autumn leads to an increase in TSM [43], which makes the

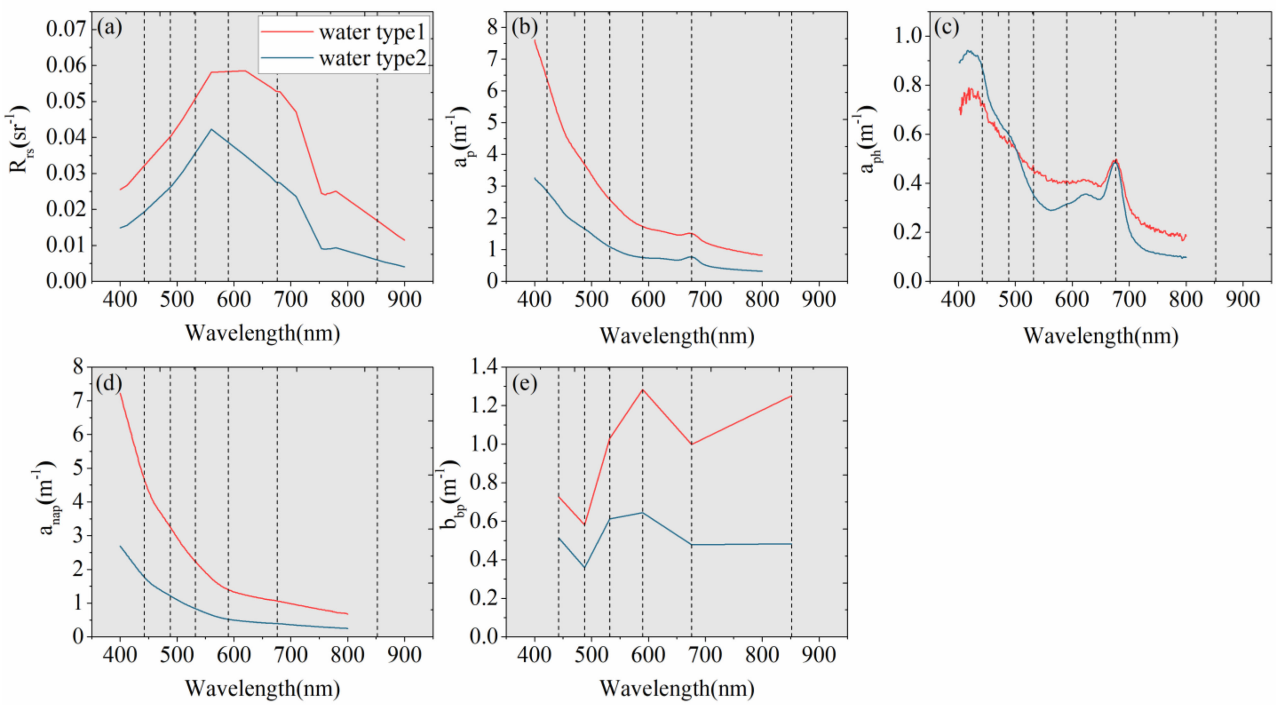

Fig. 12. Mean spectra of (a) remote sensing reflectance, (b) total particulate matter, (c) phytoplankton, (d) nonalgal particulate matter, and (e) particulate backscattering characteristics for water type 1 and water type 2. The vertical dashed lines in the figure correspond to the wavelengths of six bands measured by HS6.

seasonal variation of $b_{bp}(676)$ in these two regions different from other regions in Lake Taihu. The seasonal variation of $b_{bp}(676)$ in Lake Hongze was significantly different from that of Lake Taihu, which was demonstrated as lower $b_{bp}(676)$ in spring and winter, and higher in summer and autumn. Rainfall is one of the main factors affecting the concentration of TSM in Lake Hongze, and summer and autumn are exactly the rainy seasons. Rain causes a large number of small particles to enter the lake, resulting in higher $b_{bp}(676)$ in Lake Hongze in these two seasons. The monthly changes in $b_{bp}(676)$ of Lake Taihu and Lake Hongze from June 2016 to May 2020 are shown in Fig. 11. Fig. 11 showed that $b_{bp}(676)$ has not changed significantly in Lake Taihu in these five years, but the $b_{bp}(676)$ in Lake Hongze has decreased significantly from 2016 to 2017. Sand mining activities have been prohibited since 2017, and the TSM concentration is thus observably lower than that during sand mining activities [48], [49]. Furthermore, it was also observed that the small particles are significantly reduced [24], which will also lead to a remarkable reduction of $b_{bp}(676)$.

V. Discussion

A. Optical Characteristics of Water Type 1 and Water Type 2

The optical features of the two water types were extensively studied. The remote sensing reflectance spectra of both water types are shown in Fig. 12(a), and there are significant differences in shape and magnitude between the two water types. The remote sensing reflectance of water type 1 was higher than that of water type 2, especially in near-infrared bands. Besides, the variation of remote sensing reflectance for water type 1 was relatively low from 560 to 681 nm, whereas in water type 2, there was a remarkable decrease of remote sensing reflectance within this wavelength range. In inland water, due to the weak absorption of pigment and strong particulate backscattering, there is generally a reflectance peak at 560 nm [50], [51]. However, when the concentration of TSM increases to a certain extent, the reflectance will reach saturation within the shortwave wavelength range, and the peak position will move toward the longer wavelength and gradually appear in the red band [52]–[54]. In high TSM concentration water, the remote sensing reflectance at 620 nm, or even 665 nm, is almost always greater than that in blue and green bands [35], [55], mainly due to the enhanced backscattering caused by sediments or nonalgae particles [12], [56]. Therefore, the ratio of $R_{rs}(560)/R_{rs}(620)$ was used to determine the water types. In water type 1, the ratio was less than or approximately equal to 1, whereas the ratio of $R_{rs}(560)/R_{rs}(620)$ of water type 2 was greater than 1. At the same time, the remote sensing of reflectance at 754 nm is usually used to distinguish highly turbid water due to the strong particulate backscattering at 754 nm [57], [58]. As a result, the remote sensing of reflectance at 754 nm was also adopted to classify water types. Balasubramanian *et al.* [12] determined the water type with reflectance at 754 nm greater than 0.01 sr^{-1} as highly turbid water when developing inversion algorithms for total suspended solids in inland and nearshore coastal waters. In this study, this threshold was recalibrated and set to 0.019 sr^{-1} to distinguish the two water types, and the remote sensing

reflectance at 754 nm of water type 1 was generally higher than that of water type 2.

The average absorption spectra of total particulate matter, phytoplankton, and nonalgal particulate matter of the two water types are illustrated in Fig. 12(b)–(d), respectively, and the particulate backscattering characteristics of the particles are shown in Fig. 12(e). It can be seen that there were obvious differences in magnitude in the absorption spectra of total particulate matter and nonalgal particulate matter, especially in the total absorption, and the absorption of total particulate matter and nonalgal particulate matter at wavelengths from 400 to 800 nm in water type 1 was significantly higher than that in water type 2, whereas the absorption spectral shapes in the two water types were quite similar. However, the phytoplankton absorption spectra in the two water types presented no significant difference, as shown in Fig. 12(c). The particulate backscattering spectra in two water types are shown in Fig. 12(e), and it can be read that the particulate backscattering in the water type 1 is much higher than that in water type 2, and the particulate backscattering peak at 590 nm can be found in both water types. The largest particulate backscattering deviations between two water types were found to be at 532 and 590 nm, which may be caused by a significant difference in the concentration of inorganic small particles. It was known that small particles play a crucial role in particulate backscattering intensity at these wavelengths [59], [60]. However, the particulate backscattering at 852 nm is markedly stronger than that at 676 nm in water type 1, whereas in water type 2, the particulate backscattering at these wavelengths varies slightly. In fact, the spectra of backscattering will show spectral depressions in the particle absorption region, and as well form the peaks at the long-wavelength side of the strong absorption region [61]. Bricaud *et al.* [62] found that the backscattering spectrum of phytoplankton is opposite to the absorption spectrum, and the dip of backscattering often appears near the peak of absorption. It was also found that that pigment absorption will significantly affect the particulate backscattering intensity [63], [64] resulting in a low particulate backscattering intensity in bands with strong pigment absorption, such as 442 and 676 nm. The particulate backscattering dips at 442 and 676 nm appeared in our particulate backscattering spectrum due to the strong absorption of particulate matter and strong absorption of pigment. Therefore, it is difficult to simulate the changes in backscattering at all bands in inland water only using a monotonic power-law function. Regarding the characteristics of the backscattering spectrum shape of particles in inland water, the trigonometric function was explored to simulate the particle's backscattering spectral feature.

B. Algorithm's Sensitivity to Remote Sensing Reflectance Uncertainties

Atmospheric correction is one of the main reasons for the uncertainty of remote sensing reflectance, which will lead to the estimation results deviation by using the proposed algorithm [12], [65]. Therefore, systematic errors ranged from –20% to +20% were added to each used band to discuss the sensitivity of the algorithm. As the systematic error of the remote sensing reflectance at each band changes, the variation of the algorithm's MAPE at each band is shown in Fig. 13. It can be seen that the estimated backscattering coefficients at 442 and 488 nm were the most sensitive to changes in remote sensing reflectance. Especially at 488 nm, as the systematic error increases, MAPE increases significantly. Furthermore, the algorithm was more sensitive to changes in remote sensing reflectance at 560, 620, 754, and 865 nm. The deviation of remote sensing reflectance at 560, 620, and 754 nm will lead to a water type misclassification, resulting in the larger errors in estimation. Especially, the remotes sensing reflectance at 865 nm was used to estimate the backscattering coefficient as a reference band of the proposed algorithm, and the estimation uncertainty at this band will propagate to the other five bands. In a word, in order to obtain more accurate temporal and spatial distribution characteristics of the backscattering coefficients on the images, it is necessary to find an optimal atmospheric correction algorithm with higher correction accuracy at the six bands.

TABLE V
ACCURACY ASSESSMENT OF THE PROPOSED ALGORITHM IN OTHER LAKES IN MLYR AND THE CHESAPEAKE BAY

Region	Number	Backscattering	R^2	MAPE (%)	RMSE (m^{-1})
Three lakes in MLYR	21	$b_{bp}(442)$	0.69	38.83	0.17
		$b_{bp}(532)$	0.76	34.33	0.13
		$b_{bp}(590)$	0.81	32.19	0.12
		$b_{bp}(676)$	0.78	44.68	0.12
		$b_{bp}(852)$	0.81	54.64	0.14
Chesapeake Bay	28	$b_{bp}(450)$	0.22	252.01	0.08
		$b_{bp}(530)$	0.26	258.47	0.08
		$b_{bp}(650)$	0.24	431.95	0.09

C. Applicability of the Developed Algorithm to Other Regions

To evaluate the applicability of the proposed algorithm, independent 21 samples collected in Gonghu Bay of Lake Taihu, Lake Shijiu, and Lake Nanyi in the middle and lower reaches of the Yangtze River (MLYR) in 2020 were used to evaluate the applicability of the algorithm in inland water. Backscattering coefficients at five bands (442, 532, 590, 676, and 852 nm) were used for validation. The accuracy assessment results were described in Table V. It can be seen that although there was a certain overestimation, relatively high accuracy has been achieved at all five bands. There is a good correlation ($R^2 > 0.65$) between the estimated results and the measured backscattering coefficients at five bands with a lower RMSE (RMSE < 0.20 m^{-1}). The validation results of three lakes in MLYR showed that the proposed algorithm could be extended to other turbid inland water. As for some clean reservoirs, such as Lake Qiandao, the applicability still needs field data to further validate.

Furthermore, 28 samples from the Chesapeake Bay obtained on SeaBASS with the backscattering coefficients at three bands (450, 530, and 650 nm) were used to evaluate the applicability of the algorithm in coastal areas. However, although the backscattering characteristics of the Chesapeake Bay in some samplings also show that the backscattering at 530 nm is slightly greater than 450 and 650 nm, the algorithm performed poorly in the Chesapeake Bay. The algorithm had a serious overestimation,

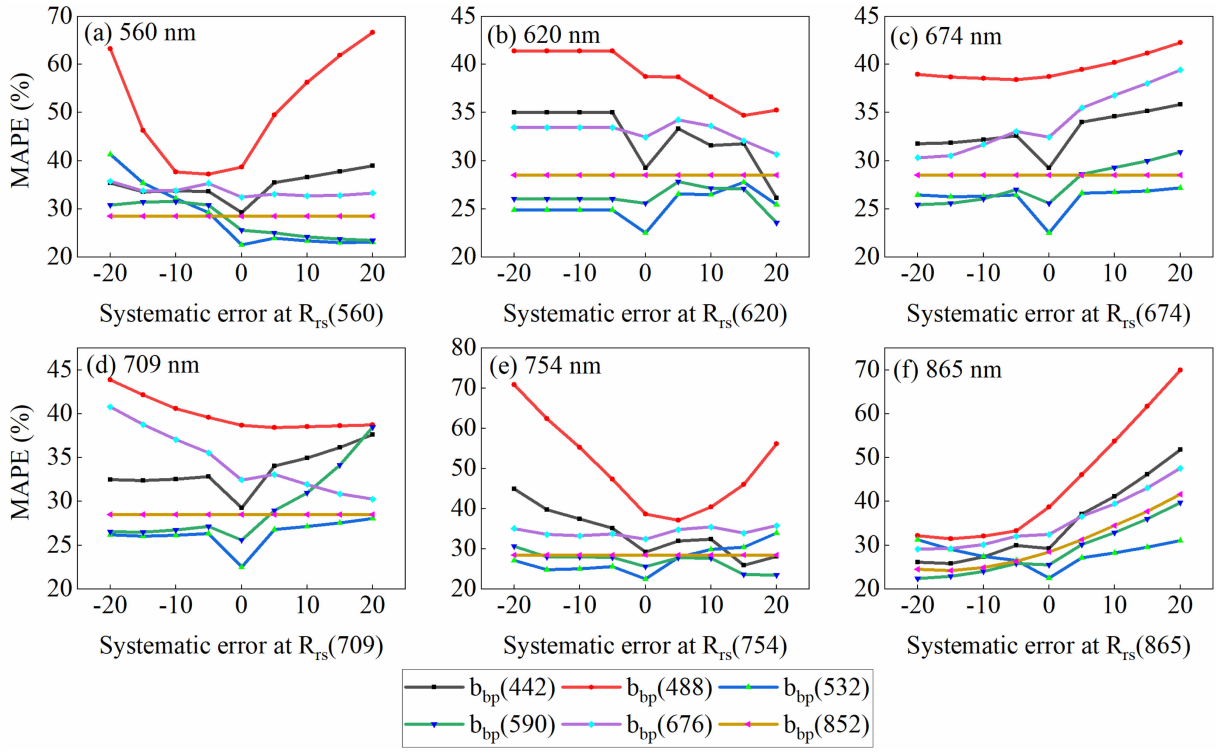

Fig. 13. MAPE of the estimation results of backscattering coefficients at six bands with the errors of remote sensing reflectance at (a) 560 nm, (b) 620 nm, (c) 674 nm, (d) 709 nm, (e) 754 nm, and (f) 865 nm.

with MAPEs $> 200\%$, and there was no good correlation between the estimated values and the measured values ($R^2 < 0.3$). Therefore, the algorithm may not be suitable for the estimation of backscattering coefficients in coastal areas, or it may be necessary to reparameterize the coefficients of the trigonometric function if used in coastal areas.

D. Relationship Between Particulate Features and Backscattering Characteristics

The concentration of suspended particles has been considered to be the main factor affecting the backscattering coefficient, and the essential characteristics of particles such as composition and size of particulate matter are the main contributors to the second-order changes in backscattering coefficient [21], [66], [67]. In previous studies, the ratio of particulate organic carbon to suspended particulate matter (POC/SPM) [68], the ratio of particulate organic matter to suspended particulate matter (POM/SPM) [69], and Chla/TSM [13], [70] have often been used as proxies of the particle composition. Therefore, the Chla/TSM ratio was chosen to indicate particle composition in this study. At the same time, the median particle diameter of the volume distribution (Dv50) is generally used to characterize the particle size [6], [68]. Before analyzing the influence of particle composition and particle size on backscattering characteristics, TSM was first adopted to normalize b_{bp} to eliminate the effect of TSM concentration. This is denoted as $b_{\mathrm{bp}}{}^*$, which is called the specific particulate backscattering coefficient. As a result, parameters of Chla/TSM and Dv50 were employed to explore the relationship between particle composition and size and the characteristics of $b_{\mathrm{bp}}{}^*$.

A correlation analysis was thus conducted between particulate features and backscattering characteristics, and the results are listed in Table VI. Consistent with the results of previous studies [1], [66], [71], TSM and ISM are the main factors affecting the change of the backscattering coefficient, with significant positive correlations at all six bands. There was a negative correlation between Chla and the backscattering coefficient at the six bands, but it was only significant at the blue band where phytoplankton has strong light absorption.

The median particle size was weakly correlated with $b_{\mathrm{bp}}{}^*$, and the absolute value of the correlation coefficient was less than 0.3. Numerous studies [67], [72], [73] have demonstrated that particle size has a negative correlation with particulate backscattering properties. However, the correlation between particle size and the specific particulate backscattering coefficient that we found in this study was not as significant as the correlation found in their study. Theoretically, the scattering angle of small particles to the incident light from the sun is larger, and the increase in the concentration of small particles will lead to increased particulate backscattering intensity [68], [74]. Meanwhile, the reduction of the particle size will lead to an increase in the scattering area, showing stronger particulate backscattering [67]. The particulate backscattering was obviously higher in water with a higher concentration of small inorganic particles, which was mainly because the assemblages with higher contributions of small-sized particles are more likely to scatter strongly [1], [59]. The particle size range we measured was too small

TABLE VI
CORRELATION COEFFICIENTS BETWEEN PARTICULATE FEATURES AND BACKSCATTERING CHARACTERISTICS

Parameters	TSM	ISM	Chla	Chla/TSM	Dv^{50}
$b_{bp}(442)$ (m^{-1})	0.55**	0.58**	-0.37**	-0.73**	-0.05
$b_{bp}(488)$ (m^{-1})	0.45**	0.47**	-0.34**	-0.58**	-0.05
$b_{bp}(532)$ (m^{-1})	0.80**	0.80**	-0.16	-0.65**	0.11
$b_{bp}(590)$ (m^{-1})	0.87**	0.86**	-0.15	-0.62**	0.16
$b_{bp}(676)$ (m^{-1})	0.86**	0.86**	-0.19	-0.65**	0.08
$b_{bp}(852)$ (m^{-1})	0.93**	0.92**	-0.05	-0.53**	0.27*
$b_{bp}^{*}(442)$ (m^2g^{-1})	-	-	-	-0.12	-0.12
$b_{bp}^{*}(488)$ (m^2g^{-1})	-	-	-	-0.15	-0.18
$b_{bp}^{*}(532)$ (m^2g^{-1})	-	-	-	-0.21*	-0.11
$b_{bp}^{*}(590)$ (m^2g^{-1})	-	-	-	-0.39**	-0.11
$b_{bp}^{*}(676)$ (m^2g^{-1})	-	-	-	-0.46**	-0.22
$b_{bp}^{*}(852)$ (m^2g^{-1})	-	-	-	-0.45**	-0.16

Note: *represents $p < 0.05$, **represents $p < 0.01$.

and most of the median particle diameter was less than 20 μm. Therefore, it may be difficult to explain the change in particulate backscattering based on particle size in a lower span, which is considered a second-order driving factor; thus, particle size did not show a significant negative correlation with specific backscattering properties. From Table VI, it can be seen that specific particulate backscattering was negatively correlated with the ratio of Chla/TSM. As the concentration of Chla increases, the absorption of phytoplankton will significantly increase. As a result, the specific particulate backscattering showed a more evident decrease with the increasing ratio of Chla/TSM. Neukermans *et al.* [69] found that POC/(POC + PIC) and POM/SPM exhibit a significant negative correlation with $b_{\mathrm{bp}}{}^{*}$ in coastal and offshore waters around Europe and French Guyana. At the same time, $b_{\mathrm{p}}{}^{*}$ was found to show a slight decrease with an increase in POC/SPM in the nearshore marine environment at Imperial Beach, California, in Wozniak's research [68]. In other words, there is generally a negative correlation between the particle composition and specific particulate backscattering intensity in inland turbid lakes, which is consistent with the results of other similar studies conducted in coastal or ocean regions.

VI. CONCLUSION

Estimating the particulate backscattering characteristics of inland water is still a challenge due to the lack of a reliable estimation algorithm suitable for inland water with complex optical properties. Based on the various characteristics of *in situ* measured backscattering with wavelength, a backscattering estimation algorithm was developed to estimated backscattering coefficients in turbid inland water. In the proposed algorithm, trigonometric functions instead of power-law functions were used to estimate the backscattering coefficients at different bands. First, according to the characteristics of the backscattering spectrum changing with TSM, $R_{\mathrm{rs}}(560)/R_{\mathrm{rs}}(620)$ and $R_{\mathrm{rs}}(754)$ were used to distinguish water types: high TSM concentration water (water type 1) and low-moderate TSM concentration water (water type 2). The backscattering coefficients at all bands of water type 1 could be simulated with a trigonometric function, whereas the backscattering features of water type 2 in the near-infrared band could be simulated with a linear function, and in the visible band, it also could be simulated with a trigonometric function. Comparison with QAA-v6, QAA-M14, QAA-750E and Gons' method showed that the accuracy of the proposed algorithm was pretty well in inland water, with all MAPEs and RMSEs in six bands being less than 40% and 0.25 m^{-1}, respectively. Finally, the proposed algorithm was successfully applied to OLCI images to obtain the spatial and temporal distribution of particulate backscattering in Lake Taihu and Lake Hongze. In Lake Taihu, $b_{\mathrm{bp}}(676)$ in winter and spring was higher than that in summer and autumn, whereas in Lake Hongze, $b_{\mathrm{bp}}(676)$ in summer and autumn was higher than that in winter and spring. The interannual variation of $b_{\mathrm{bp}}(676)$ in Lake Hongze had a significant decrease in 2017 due to the prohibition of sand mining activities. The results demonstrated that the algorithm was more sensitive to remote sensing reflectance at 560, 620, 754, and 865 nm. The developed algorithm provided an effective method for the remote sensing estimation of particulate backscattering coefficients in inland waters with complex optical properties, and can thus be further used to acquire particle information in inland waters on a large scale.

ACKNOWLEDGMENT

The authors would like to thank the ESA for providing the Sentinel-3 OLCI data and NASA-Ocean Color for providing the image process tools. The authors are grateful to all the PIs, scientists, and contributors who provide the data to the SeaBASS dataset. The authors would also like to thank the remote sensing application graduate students from Nanjing Normal University, China, for their aid with the fieldwork and lab analyses. The authors would also like to thank Yangtze River Delta Science Data Center, National Earth System Science Data Center, National Science & Technology Infrastructure of China, for the data support.

REFERENCES

[1] M. Babin, A. Morel, V. Fournier-Sicre, F. Fell, and D. Stramski, "Light scattering properties of marine particles in coastal and open ocean waters as related to the particle mass concentration," *Limnol. Oceanogr.*, vol. 48, no. 2, pp. 843–859, Mar. 2003.

[2] K. M. Bisson, E. Boss, T. K. Westberry, and M. J. Behrenfeld, "Evaluating satellite estimates of particulate backscatter in the global open ocean using autonomous profiling floats," *Opt. Exp.*, vol. 27, no. 21, pp. 30191–30203, Oct. 2019.

[3] C. Feng, J. Ishizaka, K. Saitoh, T. Mine, and H. Yamashita, "A novel method based on backscattering for discriminating summer blooms of the raphidophyte (Chattonella spp.) and the diatom (Skeletonema spp.) Using MODIS images in Ariake Sea, Japan," *Remote Sens.*, vol. 12, no. 9, May 2020, Art. no. 1504.

[4] R. Rasse, G. Dall'Olmo, J. Graff, T. K. Westberry, V. van Dongen-Vogels, and M. J. Behrenfeld, "Evaluating optical proxies of particulate organic carbon across the surface Atlantic ocean," *Frontiers Mar. Sci.*, vol. 4, pp. 1–18, 2017, doi: 10.3389/fmars.2017.00367.

[5] S. B. Wozniak, J. Meler, B. Lednicka, A. Zdun, and J. Ston-Egiert, "Inherent optical properties of suspended particulate matter in the southern Baltic sea," *Oceanologia*, vol. 53, no. 3, pp. 691–729, 2011.

[6] S. H. Lei *et al.*, "Remote sensing monitoring of the suspended particle size in Hongze Lake based on GF-1 data," *Int. J. Remote Sens.*, vol. 40, no. 8, pp. 3179–3203, Apr. 2019.

[7] W. Shi and M. Wang, "Characterization of particle backscattering of global highly turbid waters from VIIRS ocean color observations," *J. Geophys. Res., Oceans*, vol. 122, no. 11, pp. 9255–9275, 2017.

[8] H. R. Gordon *et al.*, "Spectra of particulate backscattering in natural waters," *Opt. Express*, vol. 17, no. 18, pp. 16192–16208, Aug. 2009.

[9] E. Rehm and C. D. Mobley, "Estimation of hyperspectral inherent optical properties from in-water radiometry: Error analysis and application to in situ data," *Appl. Opt.*, vol. 52, no. 4, pp. 795–817, Feb. 2013.

[10] G. F. Wu, L. J. Cui, H. T. Duan, T. Fei, and Y. L. Liu, "Specific absorption and backscattering coefficients of the main water constituents in Poyang Lake, China," *Environ. Monit. Assessment*, vol. 185, no. 5, pp. 4191–4206, May 2013.

[11] J. Lin, Z. Lee, M. Ondrusek, and X. Liu, "Hyperspectral absorption and backscattering coefficients of bulk water retrieved from a combination of remote-sensing reflectance and attenuation coefficient," *Opt. Express*, vol. 26, no. 2, pp. A157–A177, Jan. 2018.

[12] S. V. Balasubramanian *et al.*, "Robust algorithm for estimating total suspended solids (TSS) in inland and nearshore coastal waters," *Remote Sens. Environ.*, vol. 246, Sep. 2020, Art. no. 111768.

[13] K. Xue *et al.*, "Variations of suspended particulate concentration and composition in Chinese lakes observed from Sentinel-3A OLCI images," *Sci. Total Environ.*, vol. 721, Jun. 2020, Art. no. 137774.

[14] Z. Lee, K. L. Carder, and R. A. Arnone, "Deriving inherent optical properties from water color: A multiband quasi-analytical algorithm for optically deep waters," *Appl. Opt.*, vol. 41, no. 27, pp. 5755–5772, Sep. 2002.

[15] Z. Lee, B. Lubac, J. Werdell, and R. A. Arnone, "An update of the quasi-analytical algorithm (QAA_v5)," Int. Ocean Color Group Softw. Rep., 2009. [Online]. Available: https://www.ioccg.org/groups/Software_OCA/QAA_v5.pdf

[16] C. Mitchell, A. Cunningham, and D. McKee, "Remote sensing of particulate absorption coefficients and their biogeochemical interpretation: A case study in the Irish Sea," *Remote Sens. Environ.*, vol. 152, pp. 74–82, 2014, doi: 10.1016/j.rse.2014.06.003.

[17] K. Xue, R. Ma, H. Duan, M. Shen, E. Boss, and Z. Cao, "Inversion of inherent optical properties in optically complex waters using Sentinel-3A/OLCI images: A case study using China's three largest freshwater lakes," *Remote Sens. Environ.*, vol. 225, pp. 328–346, 2019, doi: 10.1016/j.rse.2019.03.006.

[18] Z. Lee, B. Lubac, J. Werdell, and R. A. Arnone, "An update of the quasi-analytical algorithm (QAA_v6)," Int. Ocean Color Group Softw. Rep., 2014. [Online]. Available: https://www.ioccg.org/groups/Software_OCA/QAA_v6_2014209.pdf

[19] P. J. Werdell *et al.*, "Unique data repository facilitates ocean color satellite validation," *EOS Trans. AGU*, vol. 84, no. 38, pp. 377–387, 2003.

[20] C. D. Mobley, "Estimation of the remote-sensing reflectance from above-surface measurements," *Appl. Opt.*, vol. 38, no. 36, pp. 7442–7455, Dec. 1999.

[21] D. Y. Sun *et al.*, "Second-order variability of inherent optical properties of particles in Bohai Sea and Yellow Sea: Driving factor analysis and modeling," *Limnol. Oceanogr.*, vol. 62, no. 3, pp. 1266–1287, May 2017.

[22] R. Ma, D. Pan, H. Duan, and Q. Song, "Absorption and scattering properties of water body in Taihu Lake, China: Backscattering," *Int. J. Remote Sens.*, vol. 30, no. 9/10, pp. 2321–2335, 2009.

[23] J. T. O. Kirk, "Estimation of the scattering coefficient of natural waters using underwater irradiance measurements," *Aust. J. Mar. Freshwater Res.*, vol. 32, no. 4, pp. 533–539, 1981.

[24] S. H. Lei *et al.*, "Remote monitoring of PSD slope under the influence of sand dredging activities in Lake Hongze based on Landsat-8/OLI data and VIIRS/DNB night-time light composite data," *IEEE J. Sel. Topics Appl. Earth Observ. Remote Sens.*, vol. 12, no. 11, pp. 4198–4212, Nov. 2019.

[25] E. W. Rice, R. B. Baird, A. D. Eaton, and L. S. Clesceri, *Standard Methods for the Examination of Water and Wastewater*. Washington, DC, USA: Amer. Public Health Assoc., 2012.

[26] S. Tassan and G. M. Ferrari, "Proposal for the measurement of backward and total scattering by mineral particles suspended in water," *Appl. Opt.*, vol. 34, no. 36, pp. 8345–8353, Dec. 20, 1995.

[27] K. G. Ruddick, F. Ovidio, and M. Rijkeboer, "Atmospheric correction of SeaWiFS imagery for turbid coastal and inland waters," *Appl. Opt.*, vol. 39, no. 6, pp. 897–912, Feb. 20, 2000.

[28] G. Liu, Y. M. Li, H. Lyu, S. Wang, C. G. Du, and C. C. Huang, "An improved land target-based atmospheric correction method for Lake Taihu," *IEEE J. Sel. Topics Appl. Earth Observ. Remote Sens.*, vol. 9, no. 2, pp. 793–803, Feb. 2016.

[29] S. Bi *et al.*, "Inland water atmospheric correction based on turbidity classification using OLCI and SLSTR synergistic observations," *Remote Sens.*, vol. 10, no. 7, Jul. 2018. Art. no. 1002.

[30] K. G. Ruddick, V. De Cauwer, Y. J. Park, and G. Moore, "Seaborne measurements of near infrared water-leaving reflectance: The similarity spectrum for turbid waters," *Limnol. Oceanogr.*, vol. 51, no. 2, pp. 1167–1179, Mar. 2006.

[31] M. Doron, S. Belanger, D. Doxaran, and M. Babin, "Spectral variations in the near-infrared ocean reflectance," *Remote Sens. Environ.*, vol. 115, no. 7, pp. 1617–1631, Jul. 15, 2011.

[32] Q. G. Xing and C. M. Hu, "Mapping macroalgal blooms in the Yellow Sea and East China Sea using HJ-1 and Landsat data: Application of a virtual baseline reflectance height technique," *Remote Sens. Environ.*, vol. 178, pp. 113–126, Jun. 2016, doi: 10.1016/j.rse.2016.02.065.

[33] C. E. Binding, D. G. Bowers, and E. G. Mitchelson-Jacob, "Estimating suspended sediment concentrations from ocean colour measurements in moderately turbid waters; the impact of variable particle scattering properties," *Remote Sens. Environ.*, vol. 94, no. 3, pp. 373–383, Feb. 2005.

[34] H. Loisel *et al.*, "Variability of suspended particulate matter concentration in coastal waters under the Mekong's influence from ocean color (MERIS) remote sensing over the last decade," *Remote Sens. Environ.*, vol. 150, pp. 218–230, Jul. 2014, doi: 10.1016/j.rse.2014.05.006.

[35] X. L. Yu *et al.*, "An empirical algorithm to seamlessly retrieve the concentration of suspended particulate matter from water color across ocean to turbid river mouths," *Remote Sens. Environ.*, vol. 235, Dec. 2019, Art. no. 111491.

[36] S. G. H. Simis, S. W. M. Peters, and H. J. Gons, "Remote sensing of the cyanobacterial pigment phycocyanin in turbid inland water," *Limnol. Oceanogr.*, vol. 50, no. 1, pp. 237–245, Jan. 2005.

[37] H. Lyu *et al.*, "A novel algorithm to estimate phytoplankton carbon concentration in inland lakes using Sentinel-3 OLCI images," *IEEE Trans. Geosci. Remote Sens.*, vol. 58, no. 9, pp. 6512–6523, Sep. 2020.

[38] Z. Lee, K. L. Carder, C. D. Mobley, R. G. Steward, and J. S. Patch, "Hyperspectral remote sensing for shallow waters. Part II. Deriving bottom depths and water properties by optimization," *Appl. Opt.*, vol. 38, no. 18, pp. 3831–3843, Jun. 1999.

[39] R. M. Pope and E. S. Fry, "Absorption spectrum (380–700 nm) of pure water. II. Integrating cavity measurements," *Appl. Opt.*, vol. 36, no. 33, pp. 8710–8723, Nov. 1997.

[40] H. J. Gons, "Optical teledetection of chlorophyll a in turbid inland waters," *Environ. Sci. Technol.*, vol. 33, no. 7, pp. 1127–1132, Apr. 1999.

[41] S. Mishra, D. R. Mishra, and Z. Lee, "Bio-Optical inversion in highly turbid and cyanobacteria-dominated waters," *IEEE Trans. Geosci. Remote Sens.*, vol. 52, no. 1, pp. 375–388, Jan. 2014.

[42] X. H. Liu, Y. L. Zhang, M. Z. Wang, and Y. Q. Zhou, "High-frequency optical measurements in Shallow Lake Taihu, China: Determining the relationships between hydrodynamic processes and inherent optical properties," *Hydrobiologia*, vol. 724, no. 1, pp. 187–201, Feb. 2014.

[43] K. Shi *et al.*, "Long-term remote monitoring of total suspended matter concentration in Lake Taihu using 250 m MODIS-Aqua data," *Remote Sens. Environ.*, vol. 164, pp. 43–56, Jul. 2015, doi: 10.1016/j.rse.2015.02.029.

[44] Y. L. Zhang, K. Shi, Y. Q. Zhou, X. H. Liu, and B. Q. Qin, "Monitoring the river plume induced by heavy rainfall events in large, shallow, Lake Taihu using MODIS 250 m imagery," *Remote Sens. Environ.*, vol. 173, pp. 109–121, Feb. 2016, doi: 10.1016/j.rse.2015.11.020.

[45] D. Liu, H. T. Duan, S. J. Yu, M. Shen, and K. Xue, "Human-induced eutrophication dominates the bio-optical compositions of suspended particles in shallow lakes: Implications for remote sensing," *Sci. Total Environ.*, vol. 667, pp. 112–123, Jun. 2019, doi: 10.1016/j.scitotenv.2019.02.366.

[46] Y. Wu, R. Dai, Y. F. Xu, J. G. Han, and P. P. Li, "Statistical assessment of water quality issues in Hongze Lake, China, related to the operation of a water diversion project," *Sustainability*, vol. 10, no. 6, Jun. 2018, Art. no. 1885.
[47] C. G. Du *et al.*, "Estimation of total phosphorus concentration using a water classification method in inland water," *Int. J. Appl. Earth Observ. Geoinf.*, vol. 71, pp. 29–42, Sep. 2018, doi: 10.1016/j.jag.2018.05.007.
[48] Z. G. Cao, H. T. Duan, L. Feng, R. H. Ma, and K. Xue, "Climate- and human-induced changes in suspended particulate matter over Lake Hongze on short and long timescales," *Remote Sens. Environ.*, vol. 192, pp. 98–113, Apr. 2017, doi: 10.1016/j.rse.2017.02.007.
[49] H. T. Duan, Z. G. Cao, M. Shen, D. Liu, and Q. T. Xiao, "Detection of illicit sand mining and the associated environmental effects in China's fourth largest freshwater lake using daytime and nighttime satellite images," *Sci. Total Environ.*, vol. 647, pp. 606–618, Jan. 2019, doi: 10.1016/j.scitotenv.2018.07.359.
[50] A. Bricaud, H. Claustre, J. Ras, and K. Oubelkheir, "Natural variability of phytoplanktonic absorption in oceanic waters: Influence of the size structure of algal populations," *J. Geophys. Res.-Oceans*, vol. 109, no. C11, Nov. 2004, Art. no. C11010.
[51] J. Lin *et al.*, "A two-step approach to mapping particulate organic carbon (POC) in inland water using OLCI images," *Ecol. Indicators*, vol. 90, pp. 502–512, Jul. 2018, doi: 10.1016/j.ecolind.2018.03.044.
[52] D. Doxaran *et al.*, "Retrieval of the seawater reflectance for suspended solids monitoring in the East China Sea using MODIS, MERIS and GOCI satellite data," *Remote Sens. Environ.*, vol. 146, pp. 36–48, Apr. 2014, doi: 10.1016/j.rse.2013.06.020.
[53] B. Han *et al.*, "Development of a semi-analytical algorithm for the retrieval of suspended particulate matter from remote sensing over clear to very turbid waters," *Remote Sens.*, vol. 8, no. 3, Mar. 2016, Art. no. 211.
[54] Y. Luo *et al.*, "Saturation of water reflectance in extremely turbid media based on field measurements, satellite data and bio-optical modelling," *Opt. Express*, vol. 26, no. 8, pp. 10435–10451, Apr. 2018.
[55] F. Shen, M. S. Salama, Y. X. Zhou, J. F. Li, Z. B. Su, and D. B. Kuang, "Remote-sensing reflectance characteristics of highly turbid estuarine waters–A comparative experiment of the Yangtze River and the Yellow River," *Int. J. Remote Sens.*, vol. 31, no. 10, pp. 2639–2654, 2010.
[56] P. Gernez, L. Barille, A. Lerouxel, C. Mazeran, A. Lucas, and D. Doxaran, "Remote sensing of suspended particulate matter in turbid oyster-farming ecosystems," *J. Geophys. Res.-Oceans,* vol. 119, no. 10, pp. 7277–7294, Oct. 2014.
[57] A. A. Gitelson *et al.*, "A simple semi-analytical model for remote estimation of chlorophyll-a in turbid waters: Validation," *Remote Sens. Environ.*, vol. 112, no. 9, pp. 3582–3593, Sep. 15, 2008.
[58] G. J. Jiang, S. A. Loiselle, D. T. Yang, R. H. Ma, W. Su, and C. J. Gao, "Remote estimation of chlorophyll a concentrations over a wide range of optical conditions based on water classification from VIIRS observations," *Remote Sens. Environ.*, vol. 241, no. 4, May 2020, Art. no. 111735.
[59] D. Stramski, M. Babin, and S. B. Wozniak, "Variations in the optical properties of terrigenous mineral-rich particulate matter suspended in seawater," *Limnol. Oceanogr.*, vol. 52, no. 6, pp. 2418–2433, Nov. 2007.
[60] D. Y. Sun *et al.*, "Light scattering properties and their relation to the biogeochemical composition of turbid productive waters: A case study of Lake Taihu," *Appl. Opt.*, vol. 48, no. 11, pp. 1979–1989, Apr. 2009.
[61] J. R. V. Zaneveld and J. C. Kitchen, "The variation in the inherent optical properties of phytoplankton near an absorption peak as determined by various models of cell structure," *J. Geophys. Res.*, vol. 100, no. C7, pp. 13309–13320, 1995.
[62] A. Bricaud, A. Morel, and L. Prieur, "Optical efficiency factors of some phytoplankters1," *Limnol. Oceanogr.*, vol. 28, no. 5, pp. 816–832, Sep. 1983.
[63] D. Stramski, A. Bricaud, and A. Morel, "Modeling the inherent optical properties of the ocean based on the detailed composition of the planktonic community," *Appl. Opt.*, vol. 40, no. 18, pp. 2929–2945, Jun. 2001.
[64] A. L. Whitmire, W. S. Pegau, L. Karp-Boss, E. Boss, and T. J. Cowles, "Spectral backscattering properties of marine phytoplankton cultures," *Opt. Express*, vol. 18, no. 14, pp. 15073–15093, Jul. 2010.
[65] N. Pahlevan, J.-C. Roger, and Z. Ahmad, "Revisiting short-wave-infrared (SWIR) bands for atmospheric correction in coastal waters," *Opt. Express*, vol. 25, no. 6, pp. 6015–6035, Mar. 2017.
[66] V. Martinez-Vicente, P. E. Land, G. H. Tilstone, C. Widdicombe, and J. R. Fishwick, "Particulate scattering and backscattering related to water constituents and seasonal changes in the Western English Channel," *J. Plankton Res.*, vol. 32, no. 5, pp. 603–619, May 2010.
[67] W. H. Slade and E. Boss, "Spectral attenuation and backscattering as indicators of average particle size," *Appl. Opt.*, vol. 54, no. 24, pp. 7264–7277, Aug. 20, 2015.
[68] S. B. Wozniak *et al.*, "Optical variability of seawater in relation to particle concentration, composition, and size distribution in the nearshore marine environment at Imperial Beach, California," *J. Geophys. Res.-Oceans*, vol. 115, no. C8, pp. 1–19, Aug. 2010.
[69] G. Neukermans, H. Loisel, X. Meriaux, R. Astoreca, and D. Mckee, "In situ variability of mass-specific beam attenuation and backscattering of marine particles with respect to particle size, density, and composition," *Limnol. Oceanogr.*, vol. 57, no. 1, pp. 124–144, Jan. 2012.
[70] D. Y. Sun *et al.*, "A semi-analytical approach for detecting suspended particulate composition in complex turbid inland waters (China)," *Remote Sens. Environ.*, vol. 134, pp. 92–99, Jul. 2013, doi: 10.1016/j.rse.2013.02.024.
[71] E. Boss *et al.*, "Comparison of inherent optical properties as a surrogate for particulate matter concentration in coastal waters," *Limnol. Oceanogr.-Methods*, vol. 7, no. 11, pp. 803–810, Nov. 2009.
[72] E. Boss and W. S. Pegau, "Relationship of light scattering at an angle in the backward direction to the backscattering coefficient," *Appl. Opt.*, vol. 40, no. 30, pp. 5503–5507, Oct. 2001.
[73] H. Loisel, J. M. Nicolas, A. Sciandra, D. Stramski, and A. Poteau, "Spectral dependency of optical backscattering by marine particles from satellite remote sensing of the global ocean," *J. Geophys. Res.-Oceans*, vol. 111, no. C9, Sep. 2006, Art. no. C09024.
[74] R. A. Reynolds, D. Stramski, V. M. Wright, and S. B. Wozniak, "Measurements and characterization of particle size distributions in coastal waters," *J. Geophys. Res.-Oceans*, vol. 115, no. C8, Aug. 25, 2010, Art. no. C08024.

Jiafeng Xu received the B.S. degree in ocean technology from Shanghai Ocean University, Shanghai, China, in 2018. He is currently working toward the Ph.D. degree in remote sensing of environment with Nanjing Normal University, Nanjing, China.

His current research focuses on the remote sensing of inland water color and optical properties in optically complex water bodies.

Yingchun Bian received the B.S. degree in geographic information system, in 2019, from Nanjing Normal University, Nanjing, China, where he is currently working toward the master's degree in remote sensing of environment.

His current research focuses on the remote sensing of clarity in inland waters.

Heng Lyu received the B.S. degree in forestry from Northwest A&F University, Xianyang, China, in 1998, the M.S. degree in forest remote sensing from Nanjing Forest University, Nanjing, China, in 2001, and the Ph.D. degree in remote sensing of the environment from the Graduate School of Chinese Academy of Sciences, Nanjing, China, in 2004.

From 2004 to 2007, he was an Assistant Professor with the Nanjing Institute of Geography and Limnology, Chinese Academy of Sciences. He is currently a Professor with Nanjing Normal University, Nanjing. His research interests include remote sensing of forest ecology and water environment.

Song Miao received the B.S. degree in geographic information system from Shandong Jianzhu University, Shandong, China, in 2016, and the Ph.D. degree in environmental remote sensing from Nanjing Normal University, Nanjing, China, in 2021.

His current research focuses on the remote sensing of lake environments.

Yunmei Li received the B.S. degree in mathematics from Yunnan University, Kunming, China, in 1987, and the Ph.D. degree in remote sensing technology and application from Zhejiang University, Hangzhou, China, in 2001.

From 2001 to 2003, she was a Postdoctoral Researcher with Nanjing Normal University, Nanjing, China, where she was an Associate Professor from 2003 to 2007. Since 2007, she has been a Full Professor of remote sensing technology and application with Nanjing Normal University, where she teaches hyperspectral remote sensing, geographical information system, and water color remote sensing. She is the Head of the Watercolor Remote Sensing Laboratory, Department of Geographical Science, Nanjing Normal University. Her research interests include water color remote sensing (water component concentration retrieval, inherent optical properties of water bodies, and bio-optical modeling for optically complex waters), particularly for inland turbid lakes.

Huaiqing Liu received the B.S. degree in surveying and mapping engineering from Anhui Agricultural University, Hefei, China, in 2018. He is currently working toward the Ph.D. degree in remote sensing of environment with Nanjing Normal University, Nanjing, China.

His current research focuses on the remote sensing of lake environments.

Jie Xu received the B.S. degree in geographic science from Hubei Normal University, Huangshi, China, in 2014, the M.S. degree in environmental science from the School of Environment, Nanjing Normal University, Nanjing, China, in 2017, and the Ph.D. degree in environmental remote sensing from Nanjing Normal University, in 2021.

His current research focuses on the remote sensing research on the carbon cycle of inland waters.